



City Research Online

## City, University of London Institutional Repository

---

**Citation:** Zhang, K., Shen, Y., Palulli, R., Ghobadian, A., Nouri, J. M. & Duwig, C. (2023). Combustion characteristics of steam-diluted decomposed ammonia in multiple-nozzle direct injection burner. *International Journal of Hydrogen Energy*, 48(42), pp. 16083-16099. doi: 10.1016/j.ijhydene.2023.01.091

This is the published version of the paper.

This version of the publication may differ from the final published version.

---

**Permanent repository link:** <https://openaccess.city.ac.uk/id/eprint/30135/>

**Link to published version:** <https://doi.org/10.1016/j.ijhydene.2023.01.091>

**Copyright:** City Research Online aims to make research outputs of City, University of London available to a wider audience. Copyright and Moral Rights remain with the author(s) and/or copyright holders. URLs from City Research Online may be freely distributed and linked to.

**Reuse:** Copies of full items can be used for personal research or study, educational, or not-for-profit purposes without prior permission or charge. Provided that the authors, title and full bibliographic details are credited, a hyperlink and/or URL is given for the original metadata page and the content is not changed in any way.

---

City Research Online:

<http://openaccess.city.ac.uk/>

[publications@city.ac.uk](mailto:publications@city.ac.uk)

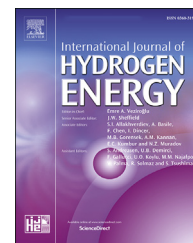
---



ELSEVIER

Available online at [www.sciencedirect.com](http://www.sciencedirect.com)

ScienceDirect

journal homepage: [www.elsevier.com/locate/hydro](http://www.elsevier.com/locate/hydro)

# Combustion characteristics of steam-diluted decomposed ammonia in multiple-nozzle direct injection burner

Kai Zhang <sup>a,\*</sup>, YaZhou Shen <sup>a</sup>, Rahul Palulli <sup>a</sup>, Ali Ghobadian <sup>b</sup>,  
Jamshid Nouri <sup>b</sup>, Christophe Duwig <sup>a</sup>

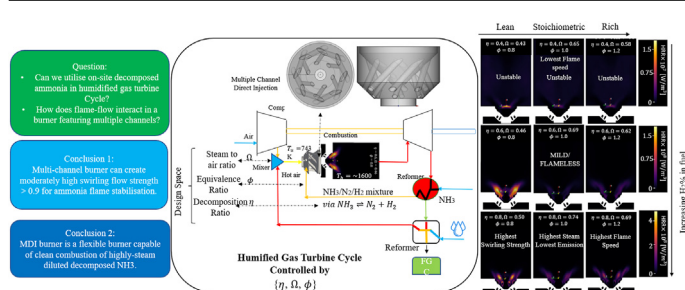
<sup>a</sup> Department of Chemical Engineering, Royal Institute of Technology (KTH), Brinellvägen 8, 114 28 Stockholm, Sweden

<sup>b</sup> Department of Engineering, City, University of London, Northampton Square, London, EC1V 0HB, UK

## HIGHLIGHTS

- Combustion characteristics of steam-diluted, decomposed ammonia is investigated.
- Swirling flow created by multiple channels features swirl number larger than 0.9.
- 80% decomposed ammonia with 74% steam-to-air ratio can stably burn in MDI burner.
- Wall heat loss leads to more  $N_2O$  for distributed flame than for conventional flame.
- $NNH$  is good flame marker for all flame regimes while  $OH$  only applies to thin flame.

## GRAPHICAL ABSTRACT



## ARTICLE INFO

### Article history:

Received 25 October 2022

Received in revised form

20 December 2022

Accepted 9 January 2023

Available online xxx

### Keywords:

Ammonia decomposition

$NO_x$  emission

## ABSTRACT

In line with the decarbonisation of power sector, carbon-free fuels are currently being investigated. In particular, green ammonia or e-ammonia is a candidate fuel which will be playing a key role in many energy-intensive industries. It calls for an in-depth understanding of eFuels combustion characteristics in the fuel flexible combustors. Therefore, the present work for the first time numerically investigates the combustion regimes of steam-diluted, decomposed  $eNH_3$  in a novel multi-nozzle direct injection (MDI) burner. Although the MDI burner is not equipped with a conventional swirler, strong flow-flame interaction is observed. The two-layer, angled channels create swirling flows featuring swirl numbers larger than 0.9 in general. The centre recirculation region can help stabilise highly steam-diluted decomposed ammonia with a maximum steam-to-air ratio of 74%.

\* Corresponding author.

E-mail addresses: [kaizhang@kth.se](mailto:kaizhang@kth.se) (K. Zhang), [yashen@kth.se](mailto:yashen@kth.se) (Y. Shen), [palulli@kth.se](mailto:palulli@kth.se) (R. Palulli), [aghobadian@city.ac.uk](mailto:aghobadian@city.ac.uk) (A. Ghobadian), [j.m.nouri@city.ac.uk](mailto:j.m.nouri@city.ac.uk) (J. Nouri), [duwig@kth.se](mailto:duwig@kth.se) (C. Duwig).

<https://doi.org/10.1016/j.ijhydene.2023.01.091>

0360-3199/© 2023 The Author(s). Published by Elsevier Ltd on behalf of Hydrogen Energy Publications LLC. This is an open access article under the CC BY license (<http://creativecommons.org/licenses/by/4.0/>).

Please cite this article as: Zhang K et al., Combustion characteristics of steam-diluted decomposed ammonia in multiple-nozzle direct injection burner, International Journal of Hydrogen Energy, <https://doi.org/10.1016/j.ijhydene.2023.01.091>

Wet combustion  
Two-stage combustion  
Flame marker  
MILD

This highest H<sub>2</sub>% containing, wettest ammonia flame case is found to emit the lowest total emission (NH<sub>3</sub>+NO + NO<sub>2</sub>+N<sub>2</sub>O) of ~400ppmvd@15%O<sub>2</sub> at stoichiometric conditions. The wall heat loss is confirmed responsible for the formation of N<sub>2</sub>O in distributed flame, suggesting the need of reducing pollution through good chamber wall insulation. However, for flames sitting in the conventional regimes, the impact of wall heat loss is found insignificant. Further, extensive data and flame regime analyses show that NNH can always accurately mark the high heat release region of all types of flames, while OH is only an effective marker for thin flames.

© 2023 The Author(s). Published by Elsevier Ltd on behalf of Hydrogen Energy Publications LLC. This is an open access article under the CC BY license (<http://creativecommons.org/licenses/by/4.0/>).

## Introduction

Electricity-derived Fuels (eFuels), such as green ammonia or e-ammonia (NH<sub>3</sub>), are promising candidates for decarbonising shipping and other industrial sectors such as the power generation sector [1]. However, ammonia's combustion properties are challenging compared to conventional fuels: its auto-ignition temperature is higher (>1000K) [2], its burning velocity is much lower (0~10 cm/s) [3], its flammability limit is narrower (equivalence ratio  $\varphi$ : 0.63–1.4) [4], and its NO<sub>x</sub> emission is often significantly higher.

To overcome these challenges, several approaches have been suggested: (a) preheating unburnt-NH<sub>3</sub> (high unburnt temperature  $T_u$ ) [5], doping with H<sub>2</sub>, or decomposing NH<sub>3</sub> [6] to increase the fuel reactivity; (b) invoking swirling flow or porous medium [7,8] for stabilising ammonia flame; (c) employing Rich-Burn, Quick-Mix, Lean-Burn (RQL) strategies to reduce fuel NO<sub>x</sub> emission and to avoid ammonia slip [9,10]; and (d) using exhaust gas recirculation to achieve MILD (Moderate or Intense Low oxygen Dilution) or FC/CDC (Flameless/Colorless Distributed Combustion) technology for pollutant reduction. In MILD combustion, wider heat release profiles (or broadened reaction zone) in the mixture fraction space inhibit the formation of local hot spots and hence reduce thermal-NO<sub>x</sub> emission [5,11–13]. These features often occur at low O<sub>2</sub>% levels [14] and the relevant combustion processes are identified as 'diffusion-ignition' dominated [15].

Among all approaches, NH<sub>3</sub> decomposition or doping with hydrogen is a very attractive method to improve the eFuel's reactivity [6,16,17]. The use of residual heat to decompose NH<sub>3</sub> on-site will undoubtedly increase the electrical efficiency of a combined power cycle. However, the approach will pose other challenges such as flashback (due to potentially large concentration of hydrogen) and overheating, inhomogeneous heat release and high combined fuel- and thermal-NO<sub>x</sub> problems to the combustion system, mostly due to the high diffusivity of H<sub>2</sub>. Of course, a combination of the different strategies can help mitigate the drawbacks. For example, in approach (d), recirculating hot steams can help avoid flashback. This is because steam dilution (1) reduced the O<sub>2</sub>% content in the reactants and lowers the flame temperature, (2) suppresses high flame speed (caused by the decomposition of ammonia); and (3) distributes the reaction zone to larger volumes and inhibits the formation of thermal-NO<sub>x</sub>. As a result, using steam to partly replace air increases electrical efficiency

and lowers the investment costs of humidified gas turbine cycles [13]. Although these are known approaches to reach clean and stable combustion, the total emissions (NO + NO<sub>2</sub> + N<sub>2</sub>O + NH<sub>3</sub>) level from burning the eFuel in today's burners is not satisfactory.

Sorrentino et al. [5] experimentally achieved non-premixed MILD combustion of preheated (300K, 600K, 900K) ammonia-air mixture at various thermal power (4 kW, 5 kW, 7 kW). In a 5 kW cyclonic burner, lean combustion results in increased NO<sub>x</sub> emission (from 250 ppm to 1000 ppm) with the increase of inlet unburnt fuel-air temperature  $T_u$ , while the NO<sub>x</sub> (<100 ppm) decreases with the increase of  $T_u$  under rich conditions (up to  $\varphi = 1.8$ ). Although low NO<sub>x</sub> emission lower than 10 ppm was also reported when  $\varphi > 1.1$ , NH<sub>3</sub> slip can exceed 1000 ppm. Besides, they compared the partial emission (NO<sub>x</sub> + NH<sub>3</sub>) at  $\varphi = 1.0$  with those reported in Kobayashi's (~2200 ppm) [19] and Valera-Medina's (~1200 ppm) [20] group and claimed a lower emission in their cyclonic burner (~200 ppm). The comparison ignored the N<sub>2</sub>O due to its "expected low" emission level (<10% of total emission) reported in Ref. [19]. However, note that N<sub>2</sub>O contributes 300 times stronger to the greenhouse effect than CO<sub>2</sub>, hence attention should also be given to this pollutant [21].

To understand this pollutant, Mashruk et al. [22] recently reported N<sub>2</sub>O emission from premixed combustion of different NH<sub>3</sub>-H<sub>2</sub> blends in an 8 kW tangential burner (swirl number 1.05). The experiment was performed over wide equivalence ratios from 0.55 to 1.40. At normal operating conditions, high N<sub>2</sub>O emission (~50 ppm--~200 ppm) occurred at very lean and very rich combustion conditions, while low emission (<25 ppm) was reported for equivalence ratios between 0.7 and 1.1. High hydrogen content (NH<sub>3</sub>-H<sub>2</sub> of 70–30 vol%) flame showed low N<sub>2</sub>O emission up to  $\varphi = 1.2$  and pure ammonia flame showed ignorable N<sub>2</sub>O emission at  $\varphi = 1.4$ . The suggested equivalence ratio for burning ammonia blends was then between 1.05 and 1.20, presenting the total emissions (NO + NO<sub>2</sub>+N<sub>2</sub>O + NH<sub>3</sub>) level of ~200ppmvd@15%O<sub>2</sub>. In the other work of Mashruk et al. [23], they reported that at  $\varphi = 0.6$ , the reaction  $NH + NO \rightleftharpoons N_2O + H$  is the major source of N<sub>2</sub>O production in the flame, while the  $N_2O + H \rightleftharpoons N_2 + OH$  and  $N_2O + M \rightleftharpoons N_2 + O + M$  are the major N<sub>2</sub>O consumption reaction in the post-flame region. The NO emission alone is above ~500ppmvd @15%O<sub>2</sub> for burning different NH<sub>3</sub>/H<sub>2</sub> blends in the same tangential burner featuring higher thermal power of 10 kW, 15 kW and 20 kW. Low combustion temperature which

hinders the  $N_2O$  consumption reaction  $N_2O + H \rightleftharpoons N_2 + OH$  can cause the increase of  $N_2O$  emission [24].

For steam-diluted or wet eFuel, the recent work of Ariemma et al. [25] reported experimentally the  $NO_x$  emission in a 7 kW cyclonic burner from fuel-lean ( $\phi = 0.6$ ) to fuel-rich ( $\phi = 1.8$ ) combustion at atmospheric conditions. Under premixed and non-premixed conditions, lean combustion presents high sensitivity to steam addition that high  $H_2O\%$ vol (volumetric) in  $NH_3-H_2O$  blends significantly reduces  $NO_x$  ( $NO + NO_2$ ) emission without changing too much the burning temperature. For non-premixed combustion, the  $NO_x$  is above  $\sim 100\text{ppmv}@15\% O_2$  but it is unclear what was the corresponding  $N_2O$  and  $NH_3$  emission levels. Mashruk et al. [10] from Valera-Medina's group numerically investigated the  $NO_x$  emission from a 10.4 MW RQL-burner modelled by a reactor network. High-pressure combustion of the steam-diluted, preheated  $NH_3-H_2$  (70-30 by vol%) fuel blends at 9.67 bar significantly reduced  $NO_x$  level to  $\sim 100\text{ppmv}$ . The earlier experimental work by Pugh et al. [26] reported that the steam-diluted  $NH_3-H_2$  blends reduce  $NO_x$  concentration in the flame zone attributing to the inhibited thermal production pathway via the extended Zel'dovich mechanism  $N + OH \rightarrow NO + H$ . Normal operation of the 25 kW RQL burner filled with  $NH_3-H_2$  (70-30 by vol%) fuel blends emitted  $NO_x$  ( $NO + NO_2$ ) below  $\sim 500\text{ppmv}@15\%O_2$ , while the  $N_2O$  emission level was not reported. Recently, Božo et al. [9] evaluated the  $NO_x$  emission in the same reactor network as in Mashruk et al. [10], high-pressure combustion (9.67 bar) of steam-dilution  $NH_3-H_2$  (70-30 by vol%) in the RQL-burner presented  $NO_x$  emission at  $\sim 100\text{ppmv}@15\%O_2$ , low  $N_2O$  emission at an order of  $10^{-8}$  by vol% and  $NH_3$  slip at an order of  $10^{-7}$  by vol%. Attributing to the reuse of residual heat in steam, their thermodynamic analysis showed a trigeneration cycle efficiency of  $\sim 59\%$ , much higher than that of the ammonia-hydrogen Brayton cycle.

Despite these valuable attempts to reduce  $NO_x$  emission, the advantageous approaches (a) – (d) are not fully employed. The main limitation is the lack of research on understanding the combustion characteristics of steam-diluted, decomposed ammonia. It is worth noting that the operation of the future ammonia power plant will benefit most from burning the on-site decomposed ammonia using residual heat than burning a typical  $NH_3/H_2$  composition aiming to mimic the properties of conventional fuels such as  $CH_4$ . However, as of today, the only work direct relevant to steam-diluted, decomposed ammonia is the one by Shen et al. [6] who numerically investigated the  $NO_x$  emission in a 10 kW, premixed PRECCINSTA burner. The  $NH_3/H_2/N_2$  ratio was forced to follow the decomposition reaction  $2NH_3 \rightarrow N_2 + 3H_2$  and the thermal efficiency of the burner was kept constant by co-varying the steam content in fuel. They reported that rich combustion of the steam-diluted, decomposed mixture at normal pressure benefits the reduction of  $NO_x$ , but the partial emission ( $NH_3+NO+N_2O$ ) is always at an unacceptable level of  $\sim 2000\text{ppmv}$ . The  $N_2O$  emission from the burner was found to be  $889\text{ppmv}@15\%O_2$  due to incomplete oxidation, much higher than one would estimate using the 1D flame or reactor network assumption. Due to the high emission level from the PRECCINSTA burner, there is an imperative need to examine the suitability of using other flexible burners for combusting the decomposed ammonia mixture. In fact, the  $N_2O$  emission is highly sensitive to (1) the

flame residence time and (2) the heat loss assumed for a reactor network. Below 1100K, wall heat loss inhibits  $NO$  emission, while it promotes  $N_2O$  and  $NH_3$  emissions under lean-burn conditions due to the weak thermal decomposition effect [27,28]. The burner design is therefore of key importance to emission reduction.

Further to integrating the four advantageous strategies (a) – (d) aforementioned, a first step must be taken to investigate whether the steam-diluted, decomposed ammonia can be stably combusted in a rich (for RQL setup) or lean (for direct use) burner featuring MILD or CDC regime. Although many works have investigated the MILD combustion of pure  $NH_3$  [5], steam-diluted  $NH_3$  [25],  $NH_3-CH_4$  [29], methanol [30], and biofuels [31], these studies have not tried to understand whether MILD combustion is achievable when burning decomposed ammonia.

The present work aims to fill these knowledge gaps by numerically simulating nine steam-diluted, decomposed ammonia flames in a small-scale, new-generation combustion burner, namely the multi-nozzles direct injection (MDI) burner. The MDI burner features a special non-premixed combustion design via injecting fuel and air through a central hole and multiple channels separately. The channels are oriented at certain angles creating swirling flows for flame stabilisation. This unique design can help avoid the problem of flashback for high  $H_2\%$  and the multiple channels increase the fuel-air mixing rate which is detrimental to the  $NO_x$  emission. The previous works on MDI burners have only focused on the non-reactive flows [32–34] and lean reactive hydrocarbon flows [35–38], while the potential of using MDI for steam-diluted, decomposed ammonia combustion remains largely unexplored. The unique flow characteristics in previous literature seem to imply that this burner will be a suitable candidate for acting as a 1st stage rich burner for RQL setup. Yet, it is unclear what would be the role of eFuel mixture composition on the flame regime transition (Conventional to MILD or FC/CDC as in Ref. [11]) and what would be the total emission ( $NO + NO_2+N_2O+NH_3$ ) from the burner under various conditions. It must be highlighted that there are currently no robust emission standards applicable to burning ammonia for power. Although one may weigh the emissions based on their greenhouse gas potential, the toxicity index for these pollutants is also different and the best strategy is to not ignore any of these pollutants. Hence, the total emission will be considered throughout the work.

In addition to these, the present work also aims to reveal the suitable flame markers for labelling the heat release region of the decomposed eFuel flame sitting in MILD or FC/CDC regimes. Cheng et al. [39] proposed that for  $NH_3$ -air premixed flames, the  $[NH_3][OH]$ ,  $[NH_2][O]$ , and  $[NH_2][H]$  are good flame markers, while the performance varies significantly with equivalence ratio. Zhu et al. [40] concluded that  $NH$  is a good premixed flame marker except for pure  $CH_4$ -air flames, and the mole product between  $[OH]$  and  $[CH_2O]$  is a better choice for marking the heat release magnitude. A systematic investigation of the flame marker was performed by Zhang et al. [41] for  $NH_3-H_2$ -air premixed flames at various conditions. They reported that for pure  $NH_3$ -air flame,  $NH$  is a good flame marker in lean than rich conditions, while adding  $H_2$  in the fuel mixture can push the validity of  $NH$  marker towards the

richer region. All these works concluded flame markers based on simple premixed flames, unable to be generalised for describing non-premixed turbulent flames operating under different flame regimes.

The present work contributes to the use of the steam-diluted, decomposed ammonia on-site by providing: (1) a comprehensive understanding of the eFuel flame characteristics in the MDI burner and an evaluation of the suitability of MDI being a 1st stage rich burner for future RQL setup; (2) a deep understanding of the flame regime transition as a function of  $H_2\%$  and  $H_2O\%$  in the eFuel mixture; (3) a thorough report of total emission ( $NO + NO_2 + N_2O + NH_3$ ) at various flame operating conditions, (4) a novel view of the suitable flame markers for labelling distributed flames. This paper is structured as follows. Section: Methodologies summarises the methods employed to perform the investigation. Section: Results and Discussions discusses the impact of steam-diluted, decomposed ammonia on the flow-flame characteristics. Finally, conclusions of the present work are given in Section: Conclusions with novel findings highlighted.

## Methodologies

### Direct injection burner geometry and mesh

Fig. 1 shows the schematic model MDI burner designed at KTH, Royal Institute of Technology for the stable combustion of steam-diluted ammonia. Cold flow behaviour in the same burner (except for the size of the fuel hole) was experimentally

and numerically investigated in our previous work [32]. In the present work, a fuel blend corresponding to decomposed ammonia ( $NH_3/N_2/H_2$ ) is injected through a  $D_{fuel} = 4mm$  central fuel hole. The hole is located at the centre of the swirler, which is comprised of two concentric layers of channels. Due to the difficulties to stabilise high-speed ammonia than methane flame, the fuel hole diameter in the present work is doubled compared to that in Ref. [32]. By doubling the fuel hole size, central jet velocity is reduced by four times, presenting the possibility of burning low flame speed ammonia. Steam-diluted air is injected through the two-layer channels featuring an outer and inner diameter  $D_{outer} = 0.25D_{fuel}$  and  $D_{inner} = 0.2D_{fuel}$ . Although steam dilution further decreases the burning capability of ammonia, it is a desired feature acting to replace compressed air in the humidified gas turbine cycles. It benefits not only the achievement of high cycle efficiency by lowering compressor duty (via after compressor steam injection), but also the reduction of  $NO_x$  by triggering the slow reaction controlled flameless combustion [11].

The arrangement of non-premixed air and fuel inlets also benefits the stable flameless combustion via an enhanced rate of shear mixing. At the exit of the swirler ( $D_{swirler} = 6D_{fuel}$ ), a combustion chamber of the size  $L_{chamber,x} \times L_{chamber,y} \times L_{chamber,z} \approx 51D_{fuel} \times 14D_{fuel} \times 12.5D_{fuel} = 204mm \times 56mm \times 50mm$  is attached.

A hexahedral dominant MDI mesh is obtained with SnappyHexMesh utility in OpenFOAM v6 [42]. The 'Background mesh', as shown in Fig. 1, has a cell resolution of  $\Delta = 1.8mm$  and 3 levels (Lv. 3) of mesh refinement are performed in the main heat release rate (HRR) region up to  $X = 6.4D_{fuel}$  featuring

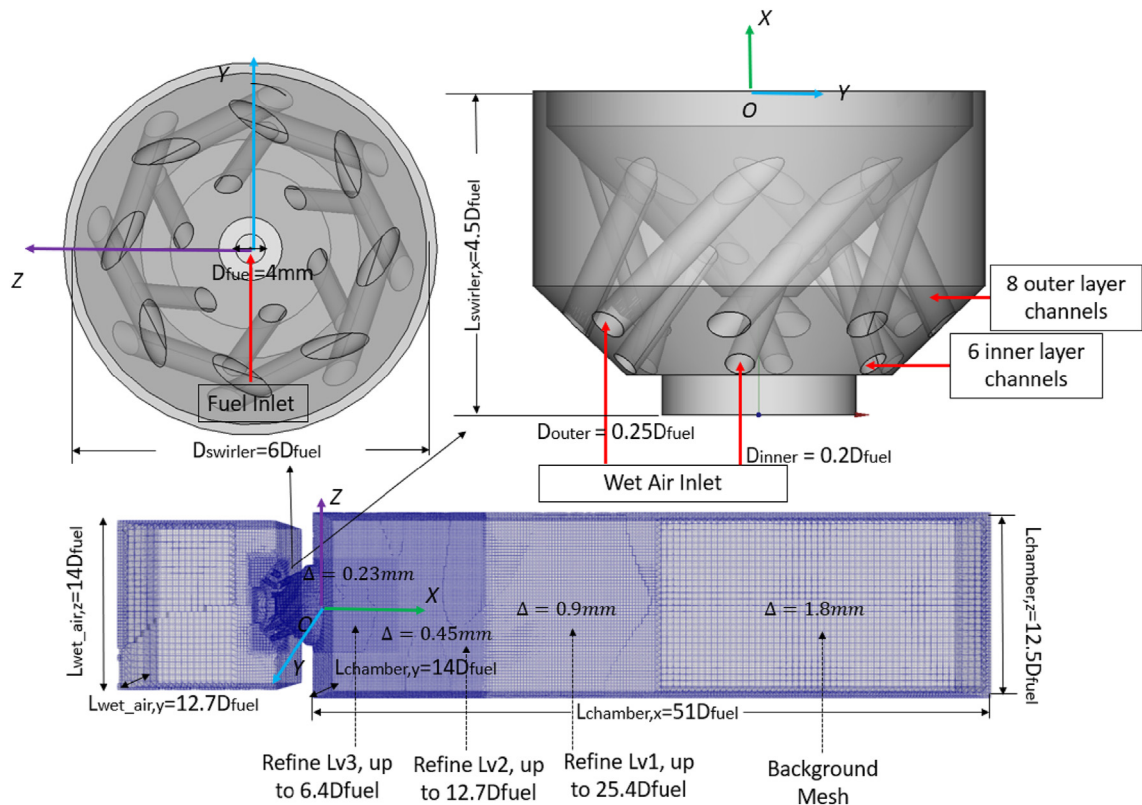


Fig. 1 – Geometric sketch and mesh information of the MDI burner.

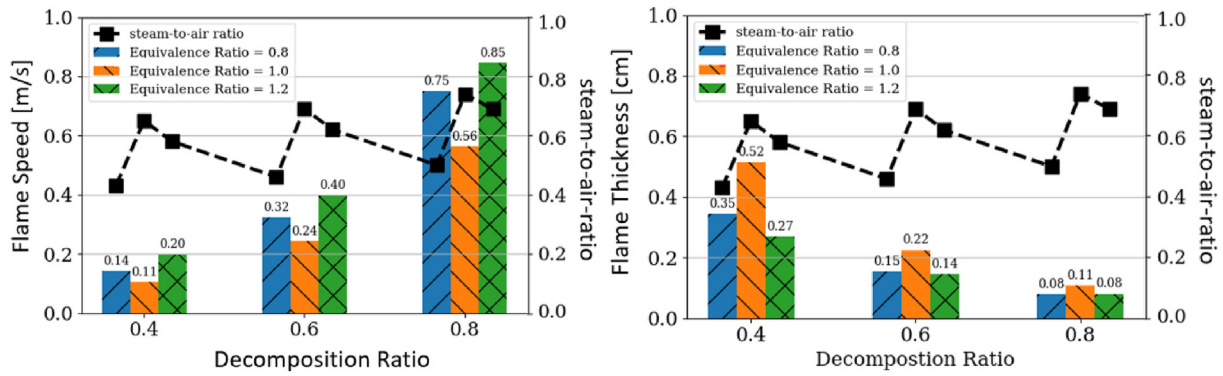


Fig. 2 – Laminar flame speed and flame thickness variation for different cases.

Table 1 – Case settings for numerical simulation of thermal power  $P_{th} = 1KW$  MDI burner.

$\eta$	$(\Omega, \varphi)$	$X_{O_2}$	Fuel $Y_{NH_3}/Y_{N_2}/Y_{H_2}$	Steam-diluted air $Y_{H_2O}/Y_{N_2}/Y_{O_2}$	$U_{fuel}$	$U_{wet\_air}$	$U_{channel}$	Swirl number
–	–	–	–	–	m/s	m/s	m/s	–
0.4	(0.43, 0.8)	0.107	0.75/0.21/0.04	0.30/0.54/0.16	16	0.49	37.5	0.95
0.4	(0.65, 1.0)	0.088	0.75/0.21/0.04	0.40/0.46/0.14	16	0.48	36.5	0.82
0.4	(0.58, 1.2)	0.09	0.75/0.21/0.04	0.36/0.49/0.15	16	0.38	28.6	1.39
0.6	(0.46, 0.8)	0.102	0.57/0.35/0.08	0.31/0.53/0.16	18	0.49	37.7	1.17
0.6	(0.69, 1.0)	0.084	0.57/0.35/0.08	0.41/0.45/0.14	18	0.48	36.7	1.02
0.6	(0.62, 1.2)	0.085	0.57/0.35/0.08	0.38/0.47/0.15	18	0.38	29.0	0.61
0.8	(0.50, 0.8)	0.097	0.33/0.55/0.12	0.33/0.51/0.16	20	0.50	37.9	1.31
0.8	(0.74, 1.0)	0.079	0.33/0.55/0.12	0.43/0.44/0.13	20	0.48	36.9	1.16
0.8	(0.69, 1.2)	0.079	0.33/0.55/0.12	0.41/0.45/0.14	20	0.39	29.5	1.02

$\Delta = 0.23mm$ . The cell size is, in general, similar to the 2 million unconfined mesh used in our previous work [32] except that the region of refinement in the present work is enlarged to confine a larger temperature gradient region. It leads to a total cell number of 3.5 million with the grid independence study presented in APPENDIX A of the supplementary data. Also, note that in the present work, the fastest flame simulated has a flame thermal thickness of 0.8 mm as shown in Fig. 2 for the high  $H_2\%$  cases. This is nearly 3.5 times larger than our local cell resolution, implying an adequately resolved reaction front. In addition, as the surface area of the fuel hole is one-fourth the size of our experimental validated simulations in Shen et al. [32], the local high-velocity gradient region is well-resolved.

### Case setups

In the present work, we attempt to provide a comprehensive understanding of how steam-diluted ( $H_2O/Air$ ), decomposed ammonia ( $NH_3/H_2/N_2$ ) burns in the flexible MDI burner. The decomposed ammonia and steam-diluted air enter the combustion chamber separately, hence primarily non-premixed flames occur. The non-premixed feature enables us to burn a large amount of hydrogen in the MDI burner, assisted also by the reduction of flame speed locally via low- $O_2$  content. A total of 9 representative cases are numerically simulated, as summarised in Table 1. The first three cases contain low  $H_2\%$ vol and high  $NH_3\%$ vol, hence the corresponding flame speed is low and the flame may extinguish (despite the high  $O_2\%$  in the

mixture). The last three cases contain high  $H_2\%$ vol and low  $NH_3\%$ vol in the fuel mixture, hence the mixtures are more reactive and local hot spots may occur to form high  $NO_x$  (despite the low  $O_2\%$  in the mixture). Fig. 2 summarises the corresponding flame speed and flame thickness for all cases.

In Fig. 2, the low flame speed at the unity equivalence ratio is worth further elaboration. The flame speed is found lower compared to the lean and rich combustion cases. This is because we attempt to keep a constant adiabatic flame temperature  $T_{ad} = 1700K$ . At the unity equivalence ratio, more steam is needed to balance the flame temperature as also seen in Fig. 2: the steam-to-air ratio. The flame speed decreases with increasing dilution by steam.

Specifically, the following assumptions are made in the present work for setting the cases in Table 1: (1) the unburnt fuel temperature is set at  $T_u = 743K$  (compressor outlet temperature), (2) the adiabatic flame temperature is set at  $T_{ad} = 1700K$  (limiting the turbine inlet temperature), and (3) the thermal power entering the MDI burner is assumed to be constant at  $P_{th} = 1KW$  for all simulations. A design space composed of three parameters: the decomposition ratio of ammonia  $\eta$ , the steam-to-air ratio  $\Omega$ , and the equivalence ratio  $\varphi$ , written as  $\{\eta, \Omega, \varphi\}$  are co-varied to satisfy the criteria (1) and (2). For the sake of clarity, APPENDIX B is provided in the supplementary data summarising how each of the parameters in the design space  $\{\eta, \Omega, \varphi\}$  is calculated. Based on these calculations, in Table 1, the central fuel velocity only changes with  $\eta$ , while the wet air velocity changes with the entire design space.

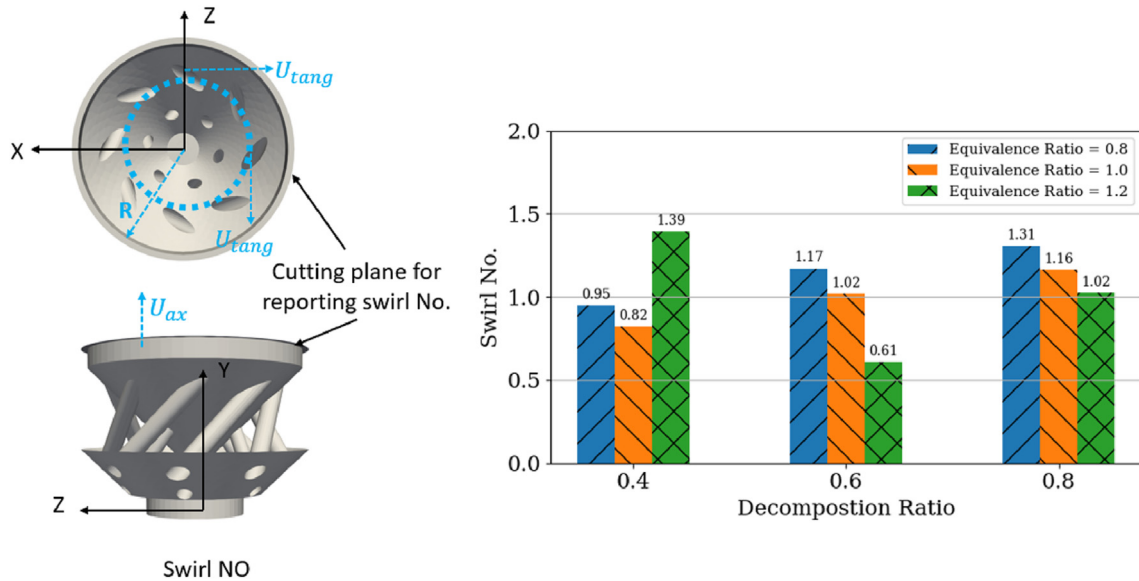


Fig. 3 – Swirl Number of different cases and the corresponding calculation plane.

### The impact of channels and flow settings on local swirl number

Swirl number has a key impact on how the flow-flame interacts and how the flame stabilises. In essence, it describes the ratio between tangential and axial velocity. Although the MDI burner does not feature a conventional swirler, the channels are oriented at angles creating swirling flow behaviour for flame stabilisation. Because of this unique design, the swirling motion is highly sensitive to flow-flame interaction. Therefore, instead of using vane angles to calculate swirl number, the present work calculates swirl number using the locally computed flow properties from numerical simulation as,

$$S = \frac{\int_0^R \rho U_{ax} U_{tang} r^2 dr}{R \int_0^R (\rho U_{ax}^2 + (p - p_{static})) r dr} \quad (1)$$

where the  $r$  is the distance of any point to the centre of a chosen plane. In Fig. 3, we explicitly label this plane and the radius  $R$  used in equation (1) is also labelled. The  $p$  in the equation is the local static pressure decoupled from the density. In our solver,  $p_{static} = p_0 = 101325pa$ . Our python script for calculating the swirl number in the Paraview environment [43] is provided in Ref. [44].

Fig. 3 shows how swirl number varies with respect to the fuel composition and the swirl numbers are also summarised in Table 1. In general, the swirling flow generated by channels features  $S > 0.9$  (except 1 case), denoting moderately strong swirling strength. Other than the anomaly case with  $\eta = 0.4$ ,  $\Omega = 0.58$ ,  $\varphi = 1.2$ , swirl number is found always increase with the increase of decomposition ratio  $\eta$ , and it decreases with

the increase of equivalence ratio  $\varphi$ . This is a very interesting observation because referring to Table 1, the fuel jet velocity  $U_{fuel}$  increases with the increase of  $\eta$  and the channel velocity  $U_{channel}$  decreases with the increase of  $\varphi$ . It indicates that for burning decomposed ammonia,  $U_{fuel}$  and  $U_{channel}$  are both positively correlated with the swirl no, i.e., either increasing fuel or air jet velocity will present a higher swirl No. It is worth reminding that the reason behind this unique behaviour is associated with the assumption of constant power and the constant adiabatic flame temperature.

For the case with  $\eta = 0.4$ ,  $\Omega = 0.58$ ,  $\varphi = 1.2$ , the swirl number of 1.39 is apparently too high and is not following the general observation. This is because the flame is not stabilised and is tending to extinguish as we will be further discussing in Section: Impact of fuel compositions on flow-flame interaction and the flame markers. The lack of combustion reduces the flow axial momentum whilst the tangential momentum remains roughly the same, resulting in a high swirl number.

### Solver and numerical settings

We numerically simulate the MDI burner using an in-house variant of reactingFoam solver incorporating the low-Mach formulation [11,45–47]. Under this formulation, a reference pressure  $p_0$  is used to calculate the mixture density using the state equation  $\bar{p} = (\bar{p}_0/RT)$ . Here, the  $R$ ,  $T$ , and  $\rho$  are the specific universal gas constant, the mixture temperature, and the density respectively. The low-Mach formulation, which decouples density from thermodynamic pressure improves the stability of the reactingFoam solver and mitigates numerical acoustic waves. The set of spatial LES filtered equations: the mass, momentum, species and enthalpy are given as,

$$\left\{ \begin{array}{l} \frac{\partial \bar{\rho}}{\partial t} + \frac{\partial}{\partial x_j} (\bar{\rho} \tilde{u}_i) = 0 \\ \frac{\partial (\bar{\rho} \tilde{u}_i)}{\partial t} + \frac{\partial}{\partial x_j} (\bar{\rho} \tilde{u}_i \tilde{u}_j) = -\frac{\partial}{\partial x_i} \bar{p} + \frac{\partial}{\partial x_j} (\tau_{ij}) - \frac{\partial}{\partial x_j} \bar{\rho} (\tilde{u}_i \tilde{u}_j - \tilde{u}_i \tilde{u}_j) \\ \frac{\partial (\bar{\rho} \tilde{Y}_k)}{\partial t} + \frac{\partial}{\partial x_j} (\bar{\rho} \tilde{u}_i \tilde{Y}_k) = \frac{\partial}{\partial x_j} \left( \bar{\rho} \tilde{D} \frac{\partial \tilde{Y}_k}{\partial x_i} \right) - \frac{\partial}{\partial x_j} \bar{\rho} (\tilde{u}_i \tilde{Y}_k - \tilde{u}_i \tilde{Y}_k) + \nabla \cdot \mathbf{J}_Y + \bar{\omega}_k \\ \frac{\partial (\bar{\rho} \tilde{h}_s)}{\partial t} + \frac{\partial}{\partial x_j} (\bar{\rho} \tilde{u}_i \tilde{h}_s) = \frac{\partial}{\partial x_j} \left( \bar{\rho} \tilde{\alpha} \frac{\partial \tilde{h}_s}{\partial x_i} \right) - \frac{\partial}{\partial x_j} \bar{\rho} (\tilde{u}_i \tilde{h}_s - \tilde{u}_i \tilde{h}_s) + \nabla \cdot \mathbf{J}_h + \bar{\omega}_h \end{array} \right. \quad (2)$$

where the Favre filtered quantity  $\tilde{q} = \overline{\rho q} / \bar{\rho}$  with over-bar denoting spatial filter. The  $D_k$  is the species diffusivity respectively. The  $\tau_{ij} = 2\mu \tilde{S}_{Dij} = 2\mu [\tilde{S}_{ij} - 1/3 \text{tr}(\tilde{S}_{ij})]$  with  $\tilde{S}_{ij} = (\partial \tilde{u}_i / \partial \tilde{x}_j + \partial \tilde{u}_j / \partial \tilde{x}_i) / 2$  being the filtered strain tensor and  $\text{tr}$  being the trace operator applied on the tensor matrix. Hence, the  $\tilde{S}_{Dij}$  is equivalent to the deviatoric part of the filtered strain tensor. The dynamic viscosity  $\mu$  is evaluated from the Sutherland equation with model constants fitted using the transport data of the San Diego mechanism [48,49].

The extra flux terms  $\mathbf{J}_h$  and  $\mathbf{J}_Y$  in equation (2) are written as,

$$\mathbf{J}_Y = -\bar{\rho} \tilde{D} \nabla \tilde{Y}_k + \frac{\alpha_{\text{eff}}}{Le_k} \nabla \tilde{Y}_k \quad (3)$$

$$\mathbf{J}_h = \rho \sum_{k=1}^N \tilde{h}_{s,k} \tilde{\mathbf{V}}_k \tilde{Y}_k - \alpha_{\text{eff}} \sum_{k=1}^N \tilde{h}_s \nabla \tilde{Y}_k = -\alpha_{\text{eff}} \sum_{k=1}^N \frac{\tilde{h}_s \nabla \tilde{Y}_k}{Le_k} - \alpha_{\text{eff}} \sum_{k=1}^N \tilde{h}_s \nabla \tilde{Y}_k = \alpha_{\text{eff}} \left( \frac{1}{Le_k} - 1 \right) \tilde{h}_s \nabla \tilde{Y}_k \quad (4)$$

where the flux term  $\mathbf{J}_h$  is closed by Fick's law  $\tilde{\mathbf{V}}_k \tilde{Y}_k = -D_k \nabla \tilde{Y}_k$  with  $\mathbf{V}_k$  being the friction velocity and by introducing non-unity Lewis number assumption  $Le_k = \alpha_{\text{eff}} / \rho D_k$ . The  $\alpha_{\text{eff}} = \alpha + \mu_{\text{sgs}} / \text{Sct}_{\text{sgs}}$ , where the turbulent Schmidt  $\text{Sct}_{\text{sgs}}$  is assumed as unity (same for turbulent Prandtl  $\text{Prt}_{\text{sgs}}$  as in Refs. [50,51]). The non-unity Lewis number assumption is needed due to the fast diffusion of the light hydrogen atom, i.e.,  $Le_{\text{H}_2} = 0.3$ . The  $Le_k$  are pre-tabulated for every single case in Table 1 at the flame front.

The other unresolved subgrid flux terms in equation (2) are expressed as:

$$\left\{ \begin{array}{l} \bar{\rho} (\tilde{u}_i \tilde{u}_j - \tilde{u}_i \tilde{u}_j) = \frac{2}{3} \bar{\rho} k_{\text{sgs}} \xi_{ij} - 2\mu_{\text{sgs}} \tilde{S}_{Dij} \\ \bar{\rho} (\tilde{u}_i \tilde{Y}_k - \tilde{u}_i \tilde{Y}_k) = \frac{\mu_{\text{sgs}}}{\text{Sct}_{\text{sgs}}} \frac{\partial \tilde{Y}_k}{\partial x_i} \\ \bar{\rho} (\tilde{u}_i \tilde{h}_s - \tilde{u}_i \tilde{h}_s) = \frac{\mu_{\text{sgs}}}{\text{Prt}_{\text{sgs}}} \frac{\partial \tilde{h}_s}{\partial x_i} \end{array} \right. \quad (5)$$

where the  $\xi_{ij}$  is the Kronecker delta and the subgrid viscosity  $\mu_{\text{sgs}} = C_k \rho \Delta \sqrt{k_{\text{sgs}}}$ . The sub-grid scale (SGS) kinetic energy  $k_{\text{sgs}}$  is obtained using the wall adaptive local eddy viscosity (WALE) method [52]. The  $\Delta$  is the filter size equivalent to the cubic root of cell volume.

The explicit source terms in equation (2) are given as,

$$\left\{ \begin{array}{l} \bar{\omega}_k(Y_k, T) = \kappa \dot{\omega}_k(\tilde{Y}_k, \tilde{T}) \\ \bar{\omega}_h = -\sum_{k=1}^N \tilde{h}_{s,k} \times \bar{\omega}_k(Y_k, T) = -\kappa \sum_{k=1}^N \tilde{h}_{s,k} \times \sum_i \omega_i (v'_{ki} - v''_{ki}) \end{array} \right. \quad (6)$$

where  $\kappa = \tau_c / (\tau_c + \tau_{\text{mix}}) = 1 / (1 + Da_\Delta)$  is the segregation factor describing the reacting fraction of the mixture in each computational cell. This is associated with the combustion model belonging to the partially stirred reactor modelling (PaSR) approach [7]. The model is suitable for capturing multi-regime features, i.e., the co-existence of non-premixed, premixed, and partially premixed combustion. Hence, it is chosen to simulate the present MDI burner in which these features co-exist locally. When Damkohler number  $Da_\Delta = \tau_{\text{mix}} / \tau_c \ll 1$  or  $\kappa \approx 1$ , the PaSR model recovers to the implicit LES formulation that the  $\tau_{\text{mix}} \ll \tau_c$  denotes perfectly premixed local combustion [53]. In the present work, the mixing time scale  $\tau_{\text{mix}}$  is calculated using the geometrical mean method, and the chemical time scale  $\tau_c$  is estimated using the reaction rate method [54] given as,

$$\left\{ \begin{array}{l} \tau_{\text{mix}} = C_{\text{mix}} \frac{\nu_{\text{eff}}}{\varepsilon} = \sqrt{\tau_{\text{mix},l} \tau_{\text{mix},\eta}} = \sqrt{\frac{k}{\varepsilon} \left( \frac{\mu}{\varepsilon} \right)^{1/2}} \\ \tau_c = \frac{n_r \times C_{\text{sum}}}{\sum_{n=1}^{n_r} \nu_{n_r} \text{RR}_{n_r,f}} \end{array} \right. \quad (7)$$

where  $\text{RR}_{n_r,f}$  is the forward reaction rate for each reaction  $n_r$ , and  $C_{\text{sum}}$  is the total species concentration obtained from the ideal gas law. The  $C_{\text{mix}} = 0.03$  is the model constant estimated based on the Reynolds number as in Ref. [54].

Further, in equation (6), the  $\dot{\omega}_k$  is the formation rate of species  $k$  and the  $\omega_i$  is the reaction rate of reaction  $i$ . The progress of the reaction is obtained from the Arrhenius approach with model constants accessible in the skeletal San Diego mechanism containing 19 species and 64 reactions [48,49]. The validation of the mechanism against experimental flame speed data can be found in our previous work [6]. More details of why the San Diego mechanism is preferred in the present work can be found in APPENDIX C of the supplementay data.

The equation (2) is discretized using the 2nd order accurate spatial (linear flux reconstruction) and temporal schemes. To interpolate velocity and temperature from the cell to the face centres, Gauss linear method is chosen. For species and energy interpolation, the Gauss Gamma method is used. The PISO [55] algorithm is chosen for implicit time integration containing four inner velocity corrector steps (solving Poisson's equation) to satisfy continuity after the step of the momentum predictor. The maximum Courant-Friedrich-Levy number  $Co$  is set as 0.3 with its value smaller than 0.2 in the high heat release region. The residence time of the flow in the computational domain is estimated as  $\tau_{\text{res}} = (D_{\text{swirler},x} + D_{\text{chamber},x}) / U_{\text{channel}} \approx 0.2 / 30 = 0.0067\text{s}$ . Due to the long time required for the recirculation zone to develop, we choose

to run the cases first for a physical time of  $15 \tau_{res}$  during which the monitored mixture fraction becomes steady. This is then followed by a collection of temporal statistics (averaging) for another  $15 \tau_{res}$  flow-through time.

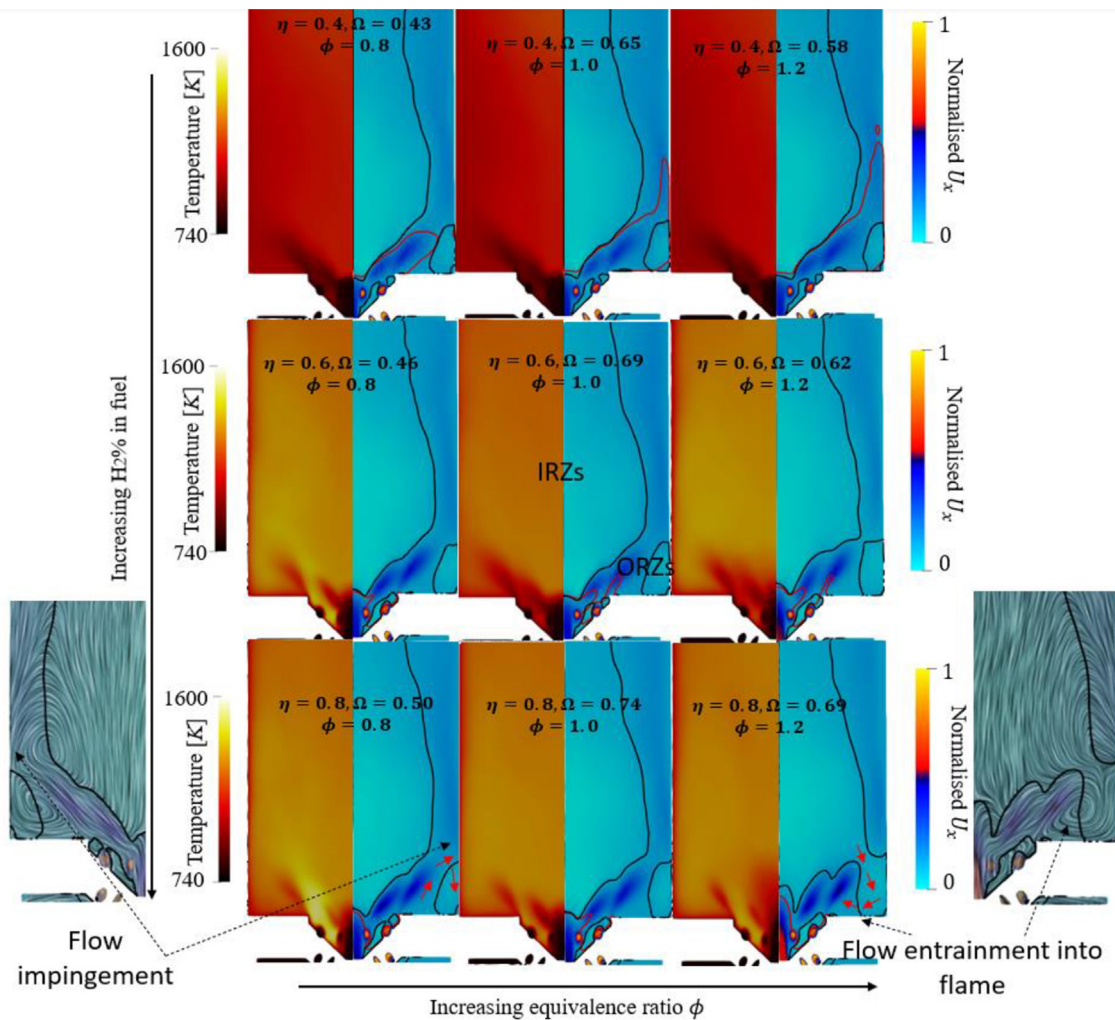
## Results and discussions

### Impact of fuel compositions on flow-flame interaction and the flame markers

Fig. 4 shows the mean streamwise velocity and temperature contour in the MDI burner. The flame root is marked using a red contour line of temperature equal to 1000K and the recirculation region is denoted with the black contour line of zero-streamwise velocity. In general, the flow fields in the MDI burner are not very sensitive to the  $\text{NH}_3$  decomposition ratio  $\eta$  and the equivalence ratio  $\phi$ . Two big inner recirculation zones (IRZs) and two small outer recirculation zones (ORZs) are always formed. However, the flame root is sensitive to the

decomposition that for cases with  $\eta = 0.4$ , a continuous reduction in flame temperature was observed in the simulation. As the simulation time iterates forward, the time-averaged 1000K flame root extends downstream. It indicates that these low  $\text{H}_2\%$  flames are extinguishing.

Besides, it is noticed that the flow field of case  $\eta = 0.8, \Omega = 0.69, \phi = 1.2$  differs from that of the other cases. Although two recirculation zones are also formed, a very strong backward flow entrainment to the flame root is observed. The backflow is responsible for delivering partially burnt products to the short flame region via the ORZs, acting to greatly stabilise this high  $\text{H}_2\%$  (80%vol of ammonia decomposed), rich flame. According to Table 1, the flame features the highest flame speed of 0.85 m/s among all cases. For lower flame speed cases, there presents a local flow impingement on the chamber wall and no intense recirculation of the partially burnt product from the side ORZ to the flame root may occur. The different flow-flame interaction is denoted in Fig. 4 with the red arrows for the lean case  $\eta = 0.8, \Omega = 0.5, \phi = 0.8$  and the rich case  $\eta = 0.8, \Omega = 0.69, \phi = 1.2$



Time-averaged flow field (streamwise velocity) and temperature.

**Fig. 4 – Flow-flame interaction. Black Line:  $U_x = 0\text{m/s}$ ; Red Line: flame root at  $T = 1000\text{K}$ . (For interpretation of the references to colour in this figure legend, the reader is referred to the Web version of this article.)**

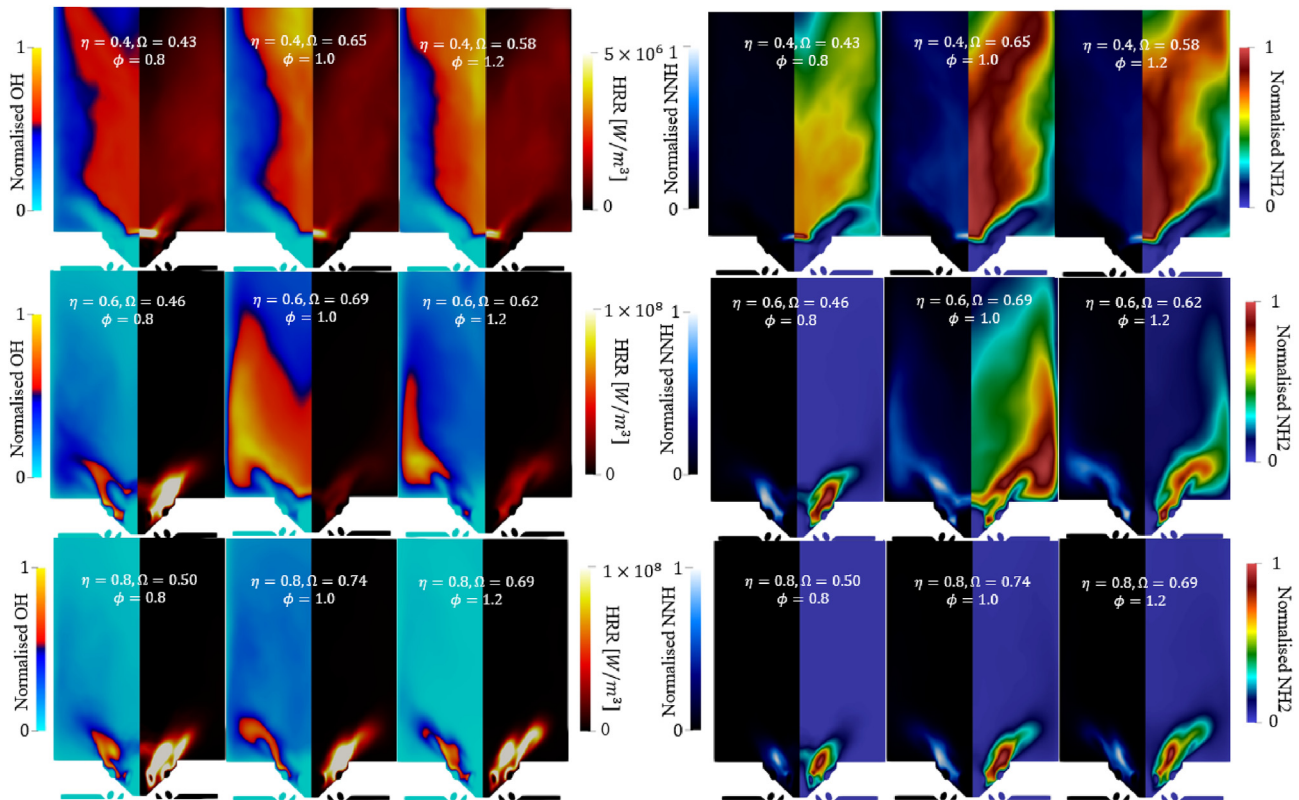


**Fig. 5 – Time-averaged species mass fraction (OH, NNH, NH<sub>2</sub>) and HRR distribution. Each image is normalised to [0, 1] using  $(Y - Y_{min}) / (Y_{max} - Y_{min})$ . Note that HRR is not normalised.**

respectively. Furthermore, a closer look at Fig. 4 shows that unless the flame root penetrates downstream as for the case with  $\eta = 0.4$ , increasing equivalence ratio always decreases the gap between the inner recirculation and outer recirculation zone. It leads to the merge of the black contour lines for the case with  $\eta = 0.8$ ,  $\Omega = 0.69$ ,  $\varphi = 1.2$ . Promoted mass flux (hot product) contribution from ORZ to flame root help stabilise more the high H<sub>2</sub>% rich flame than the low H<sub>2</sub>% lean flame. This observation is very important for reduced order modeling of the flames using 0D complex reactor network [56]. Different fractions of burnt product recirculation and hence different mass flux between the IRZ and ORZ imply practical difficulties to generalise a CRN for both high and low H<sub>2</sub>% flames.

Fig. 5 shows the mean mass fraction of OH, NNH and NH<sub>2</sub>, and the heat release rate. The species contours, except the HRR, are normalised to the maximum of each image to show the change in flame topology. We show OH, NNH, and NH<sub>2</sub> distribution because these are the three most widely used flame markers, and they are responsible for different stages of ammonia combustion. Specifically, it is known that [57] (1) NH<sub>3</sub> is first decomposed via H-abstraction reaction, followed by the NH<sub>i</sub> recombination reaction towards N<sub>2</sub> (via the N<sub>2</sub>O and NNH intermediate channels); (2) OH is the key contributor to the formation of HNO which leads to about 70% of NO production via oxidation [58]; and (3) in the DeNO<sub>x</sub> or NO re-burning process, NH<sub>2</sub> is the key NO consumption reaction through NH<sub>2</sub>+NO=H<sub>2</sub>O+N<sub>2</sub>. A qualitative observation in Fig. 5 shows that,

- (1) The flames in the first row ( $\eta = 0.4$ ) tend to extinguish due to the low flame speed of the mixture (below 0.2 m/s, refer to Fig. 2). The large distribution of OH downstream apparently indicates the unburnt nature of the fuel. Similar experimental images showing the extinguishing methane flame can be found in Ref. [54].
- (2) Steam-diluted, decomposed ammonia flame can burn stably in the 1 kW MDI for  $\eta = 0.6$  and  $\eta = 0.8$ . Neither undesired flashback nor the flame extinguishing phenomenon may occur. Flameless combustion or a distributed flame is observed for  $\eta = 0.6$ ,  $\Omega = 0.69$ ,  $\varphi = 1.0$  (refer to the size of HRR and NNH).
- (3) In lean flames where  $\varphi = 0.8$ , OH seems to be a reasonable indicator for labelling HRR, while they differ in stoichiometric and rich flame. The cause of this is that in distributed flame, OH occurs primarily in the post-reaction zone rather than in the reaction front as in thin flames.
- (4) NH<sub>2</sub> and NNH seem to be the effective flame marker for all cases except in a very distributed flame such as the  $\eta = 0.6$ ,  $\Omega = 0.69$ ,  $\varphi = 1.0$ .

To quantify the relationships between radical species and HRR, and to fill the knowledge gap of the lacking common consensus on ammonia flame marker, Fig. 6 shows the Spearman correlation  $R$  [59] between the HRR and some chosen species' mass fractions (normalised to [0, 1]). The Spearman correlation assesses monotonicity between two sets of variables with its sign indicating the direction of the

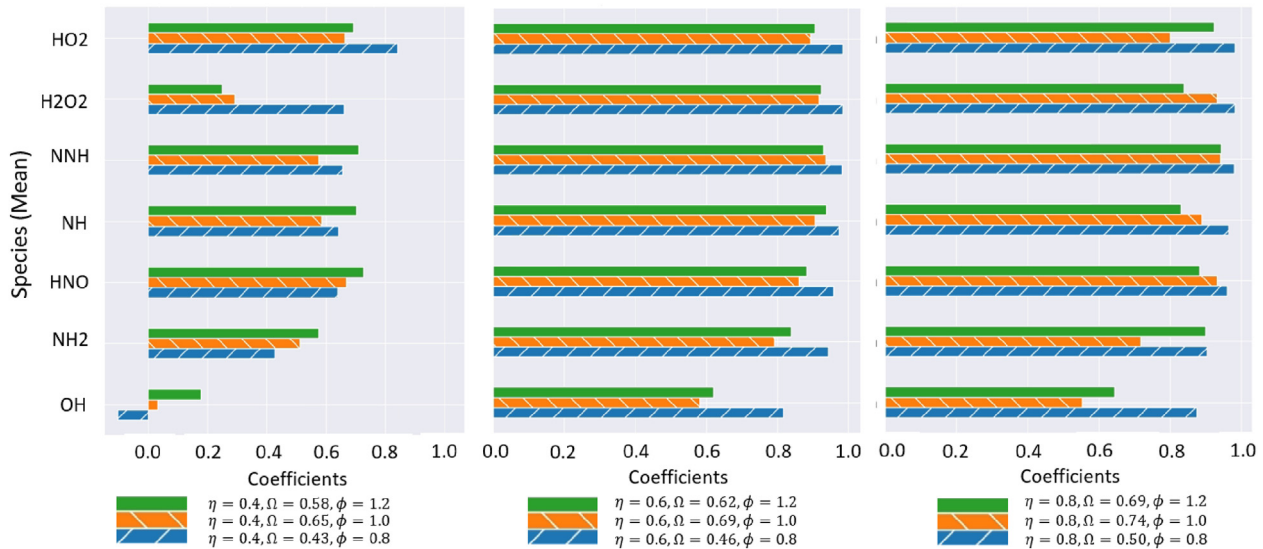


**Fig. 6 – Spearman correlation assessing the consistency between species and HRR. High coefficients indicate the effectiveness of the flame marker.**

association. Its mathematical description is the same as the Pearson correlation, given as,

$$R = \frac{\sum_{j=1}^N (HRR_j - \overline{HRR})(Y_j - \bar{Y})}{\sqrt{\sum_{j=1}^N (HRR_j - \overline{HRR})^2} \sqrt{\sum_{j=1}^N (Y_j - \bar{Y})^2}} \quad (8)$$

except that the variables used in Spearman correlation are ranked in advance. In equation (8),  $N$  is the number of cells and  $Y_j$  refers to the normalised mean mass fraction of an interesting species. The  $[\bar{\cdot}]$  represents the statistical mean of the focusing quantity. For  $R = 1$  and  $-1$ , the HRR and  $Y$  are perfectly positive and negative correlated respectively. To avoid bias induced by the numerical mesh resolution, the chosen data are mapped on a mesh containing equal cell distance before the correlation is computed.

Note that the presented correlation in 3D must differ from any similar analyses performed in 1D. The 3D flames contain multiple combustion regimes that are unseeable in either premixed or counter flame configuration. In particular, the swirl-stabilised regime to be discussed in Section: Combustion Mode Analyses does not exist in a 1D simulation. Therefore, the associated spatial distribution of N-based flame markers should not be ignored, demanding 3D Spearman correlations to be performed.

In Fig. 6, It is observed that when the decomposition ratio  $\eta$  is fixed (ignoring extinguishing flames with  $\eta = 0.4$ ),

- Many intermediate species such as  $\text{HO}_2$ ,  $\text{NNH}$ ,  $\text{NH}_2$ , and  $\text{OH}$  etc. are effective markers for HRR in lean flames (Coefficient  $R > 0.9$  for  $\phi = 0.8$ ) because these species intensively react with abundant  $\text{O}_2\%$  to release heat.
- For stoichiometric and rich flames ( $\phi = 1.0$  &  $1.2$ ), most indicative species are still effective markers except the  $\text{OH}$  (Coefficient  $R \geq 0.8$ ). The  $\text{NNH}$  is the most effective flame marker for both flames, while the  $\text{NH}_2$  is less effective for the stoichiometric flame.

It is worth highlighting that for stoichiometric flames, the correlation between  $\text{OH}$  and HRR is very low (Coefficient  $R < 0.6$ ). This is because the flames are more firmly defined in the MILD regime as will be quantified in the following section. The flame distribution nature in MILD combustion delays the production of  $\text{OH}$  from the thin reaction zone to the post-reaction zone.

### Combustion mode analyses

As shown in Fig. 7, a combustion system can be characterised into four modes: the conventional, the high temperature, the swirl stabilised, and the MILD combustion mode. The original combustion mode graph was defined based on the unburnt mixture temperature  $T_u$ , the mixture self-ignition temperature ( $T_{ign}$ ), and the maximum temperature increase ( $\Delta T = T_{max} - T_c$ ) where  $T_{max}$  is the adiabatic flame temperature [60,61]. Fooladgar et al. [50] extended the definition by replacing  $T_u$  with the local mixture temperature  $T_c$ , and used local mixture's self-ignition temperature  $T_{ign}$  in their extended combustion model analysis (ECMA). The  $T_{ign}$  was calculated by evolving a one-dimensional (in-time) perfectly stirred reactor (PSR) filled with local mixture compositions to 1s [11,60] and the  $T_{max}$  in ECMA graph was the true local maximum temperature from the computation. The ECMA graph is then capable of characterising the combustion mode/regime of local mixtures (or fluid parcels). Specifically,

- When  $\Delta T > T_{ign}$  and  $T_c < T_{ign}$ , fluid parcels sit in conventional combustion mode. The local fluid parcels are unable to self-ignite and the flame temperature increase is higher than the self-ignition temperature.
- When  $\Delta T > T_{ign}$  and  $T_c > T_{ign}$ , fluid parcels sit in high-temperature combustion mode. These parcels can self-ignite and the flame temperature increase is also high.
- When  $\Delta T < T_{ign}$  and  $T_c < T_{ign}$ , fluid parcels are either sitting out of flammability limit and are hence not ignitable, or the

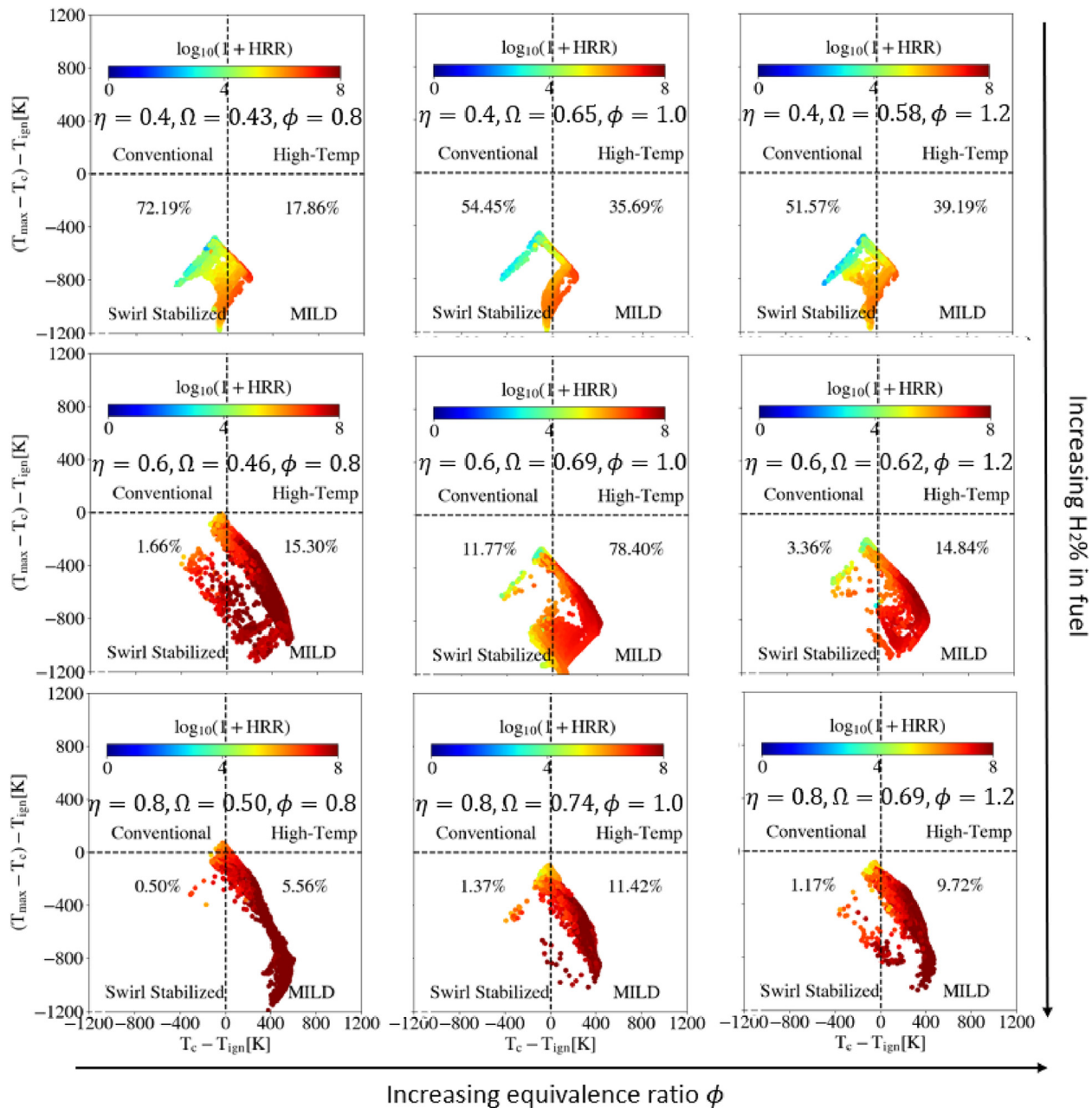


Fig. 7 – Extended combustion mode graph to quantify the flame characteristics.

preheating is not high enough for ignition and is therefore dominated by swirl-stabilised combustion. For parcels highly non-flammable,  $T_c \ll T_{ign}$  and are not viewable in Fig. 7. It explains why the sum of the percentage values in each graph is not unity (100%).

- When  $\Delta T < T_{ign}$  and  $T_c > T_{ign}$ , the flame temperature increase is lower than the parcels' self-ignition temperature, while the fluid parcels are self-ignitable. The fluid parcels sit in the MILD regime.

In Fig. 7, it is interesting to observe that.

- (a) With a low decomposition ratio of ammonia, e.g.,  $\eta = 0.4$ , a large amount of Swirl-Stabilised fluid parcels

(>50%) are observed. The observation is common for flameless or distributed combustion. However, the very low heat release ( $\log_{10}(1 + HRR) < 5$  in general) associated with these parcels indicates the flames tend to extinguish.

- (b) With medium and high decomposition ratios of ammonia, flames are stable and few Swirl-Stabilised fluid parcels are observed. The stoichiometric flames present the most fluid parcels in the MILD regime. It explains why for these flames, OH is a bad flame marker.
- (c) Comparing cases of  $\eta = 0.8$  to  $\eta = 0.6$ , there are fewer fluid parcels in the lower quadrant of the EMCA graph. The sum of percentage values is far lower than unity,

indicating the presence of more non-explosive fluid parcels.

To better understand the flame characteristics, for the first time, we choose to map the ECMA classification back on the LES plane, as given in Fig. 8. A very interesting observation is the high similarity (composed of blue and green regions) between the MILD combustion with  $\eta = 0.6, \Omega = 0.69, \phi = 1.0$  and the flame extinguishing cases with  $\eta = 0.4$ . The biggest difference is that for MILD combustion, swirl stabilised fluid parcels are found to wrap around the MILD parcels, while it is the opposite for extinguishing flames. For other flames featuring a small portion of MILD fluid parcels, non-explosive burnt fluid parcels (yellow) are formed in the vicinity of the flame tip.

Fig. 9 shows the local  $O_2\%$ vol for the fluid parcels sitting in MILD regime. The local reactant dilution is known of high importance in achieving MILD combustion and we notice that the majority of fluid parcels contain an  $O_2\%$ vol lower than

10%. For rich flame, the local temperature is lower than the lean flame, and local MILD combustion occurs at lower  $O_2\%$ .

#### Time-averaged emissions

Fig. 10 shows the emission calculated on a plane downstream of the combustion chamber where  $x = 2L_{chamber,z}$  (refer to Fig. 1). Space-averaging is performed on that plane for the time-averaged variables: NO,  $NO_2$ ,  $N_2O$  and  $NH_3$ . The calculation follows equation (9),

$$X_i [ppmvd @15\%O_2] = \frac{X_i / (1 - X_{H_2O}) \times (20.9 - 15)}{20.9 - [X_{O_2} / (1 - X_{H_2O})]} \times 10^6 \quad (9)$$

where ppmvd stands for parts per million, volume, dry-based, and  $X_i$  represents the space- and time-averaged species molar fraction. For all cases excluding the extinguishing ones, the  $NO_2$  emission is very low compared to other emissions, hence it is not shown independently. From Fig. 10, it is found that,

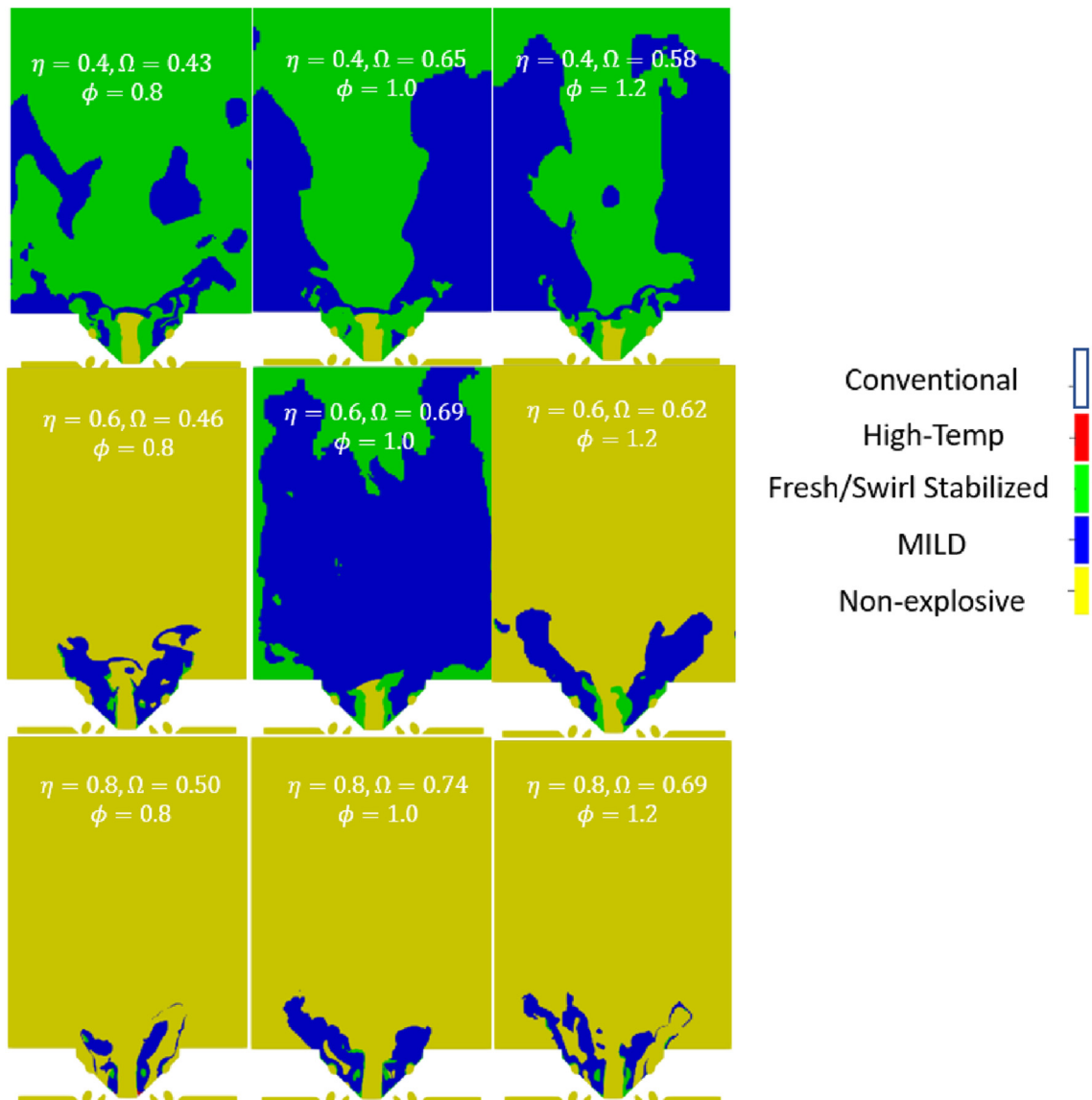


Fig. 8 – Instantaneous LES plane showing the ECMA classification.

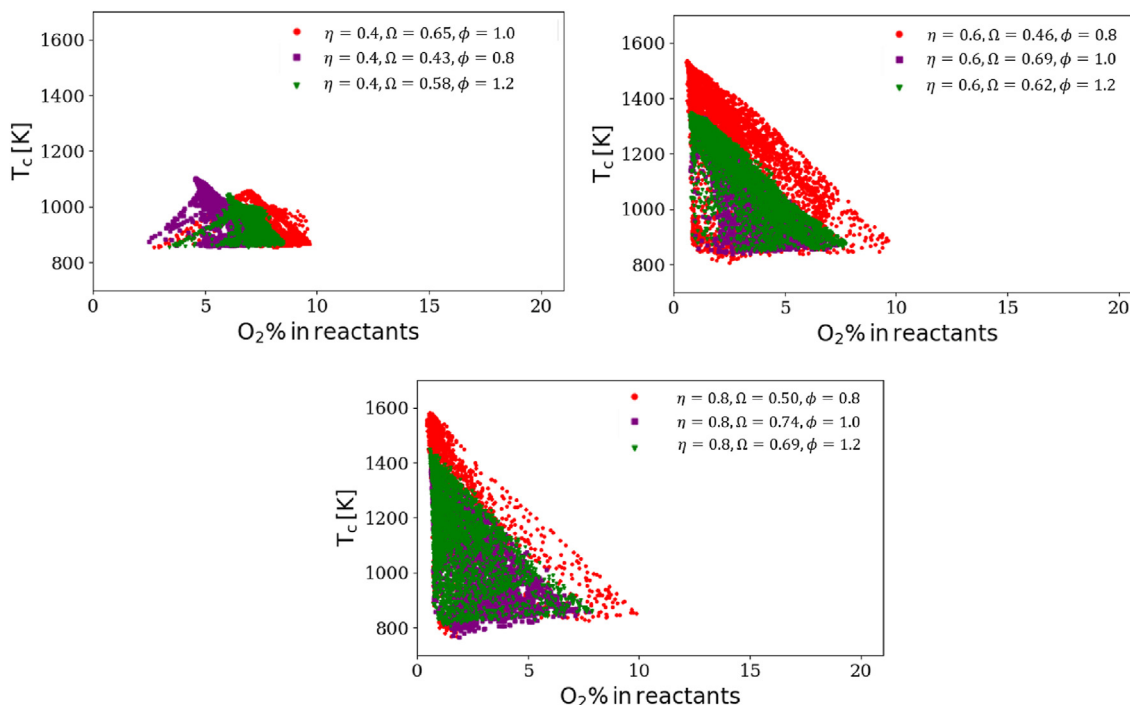


Fig. 9 – The instantaneous  $O_2\%vol$  for the local fluid parcels sitting in MILD regime.

- (1) Rich burn of steam-diluted, decomposed ammonia emits much lower NO than lean burn. However, rich burn emits a large amount of undesired  $NH_3$  due to incomplete combustion. It implies the need of using a 2nd stage lean burner for complete oxidisation. For rich combustion of 80% decomposed ammonia, the  $N_2O$  level is in general at an acceptable level that a 2nd stage lean burner will aid the pollutant reduction. For rich combustion of 60% decomposed ammonia, the tripled  $N_2O$  emission is undesired, while a well-designed RQL burner may still aid the pollutant reduction since there is also a high  $NH_3$  emission which can provide free H radicals in a 2nd stage lean burner.
- (2) Lean burn of steam-diluted, decomposed ammonia is not suggested that the more ammonia is decomposed (i.e., more  $H_2$  in fuel blend), the more NO is emitted. The total emissions of NO,  $NO_2$ , and  $N_2O$  are at an unacceptable level.
- (3) Stoichiometric combustion of steam-diluted, 80% decomposed ammonia ( $\eta = 0.8, \Omega = 0.74, \phi = 1.0$ ) is promising. Despite the slightly high  $N_2O$  emission than rich burning of the steam-diluted, 80% decomposed ammonia ( $\eta = 0.8, \Omega = 0.69, \phi = 1.2$ ), the ratio between the  $NH_3$  and  $(NO + NO_2 + N_2O)$  is below unity, presenting  $NH_3$  emission at 164ppmv @15% $O_2$ . Amongst all possible combinations, the total emission of this case is the lowest at 408ppmv @15% $O_2$ .

To observe the local pollutant formation and consumption, the  $N_2O$  and NO emissions are presented in Fig. 11 with colourmaps normalised from zero to unity using the local maxima of the individual image. In general, high NO emission occurs where there is high HRR (refer to Fig. 5). The four lowest

NO emission cases (stoichiometric and rich cases at  $\eta = 0.6$  & 0.8) are found to present a largely distributed NO formation region, associating closely with the flame distribution. Other than the flame extinguishing cases ( $\eta = 0.4$ ), the middle case in Fig. 11 presents the largest flame region in Fig. 5 and therefore shows the lowest NO emission, demonstrating the benefit of the MILD regime on NO reduction. For  $N_2O$ , wall heat loss promotes its formation at rich than lean combustion conditions for cases of  $\eta = 0.6$ . When  $\eta = 0.8$ , wall loss impact is low probably because the  $N_2O$  is consumed by the abundant H radicals already produced in the short main flame region.

These observations agree well with the finding by Galle et al. [62] and Okafor et al. [27,28] who reported that wall heat loss inhibits the  $N_2O$  decomposition at a temperature lower than 1100K. Indeed, the wall temperature in our simulation is set as 1000K, which may have an impact on predicting  $N_2O$  emission. In addition, cross-comparing Figs. 8, Fig. 10, and Fig. 11, we see that MILD combustion is more sensitive to the wall heat loss, i.e., high heat loss leads to high  $N_2O$  emission. This might be explained by the fact that the formation of H radicals in MILD combustion is not as intensive as that in conventional flames. The main consumption reaction of  $N_2O$  with H radicals [20] is therefore weakened in the near wall region. It indicates the need for good heat insulation to reduce  $N_2O$  emissions near the chamber wall, particularly for MILD combustion.

## Conclusions

To guide the on-site use of decomposed ammonia for power, high-fidelity large eddy simulation is employed to explore the combustion characteristics of non-premixed  $NH_3/N_2/H_2$  and

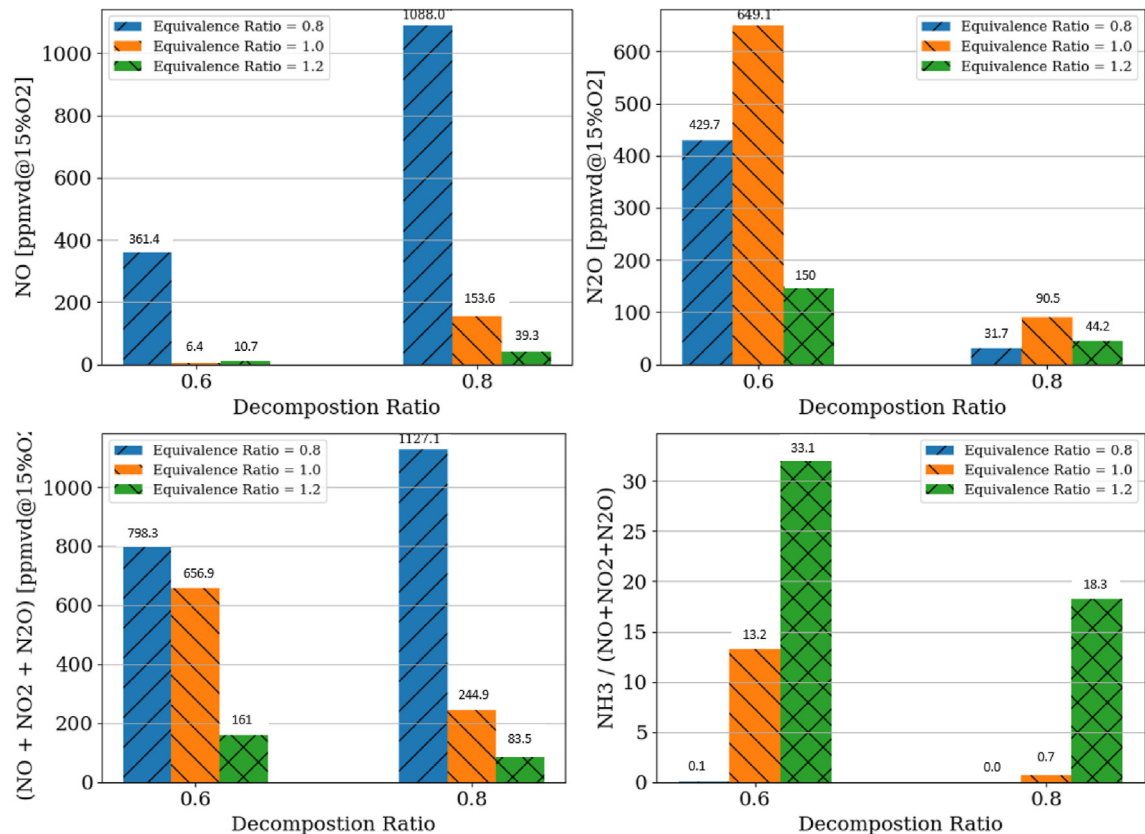


Fig. 10 – Emissions of NO, NO<sub>2</sub>, N<sub>2</sub>O, and NH<sub>3</sub> from burning steam-diluted, decomposed ammonia in a 1 kW MDI burner.

H<sub>2</sub>O/N<sub>2</sub>/O<sub>2</sub> blends in a new generation multiple-nozzle injection (MDI) burner. The work is primarily motivated by lacking the knowledge of (1) how flow-flame interacts under advantageous wet eFuel combustion environments; (2) what are the corresponding combustion regimes; and (3) what are the total emissions from the MDI burner operating under lean, stoichiometric, and rich combustion conditions. In addition, it is also motivated by the lack of generalised flame markers for labelling flames defined by different combustion regimes.

To fill the knowledge gap, finite rate chemistry is needed to track the transportation of all important species and branching reactions accurately at both lean and rich flame conditions. For this purpose, a Skeletal San Diego mechanism containing 19 species and 64 reactions is employed, accounting for key NO production and destruction reactions. Pre-setting the MDI burner to work at constant thermal power and efficiency, a design space comprising: the mass-based steam-to-air ratio  $\Omega$ , equivalence ratio  $\phi$ , and ammonia decomposition ratio  $\eta$  is used for choosing nine representative flames.

For flow-flame interaction, it is found that.

- Although the MDI burner is not equipped with a conventional swirler, the specially designed channels can create strong swirling flows featuring swirl numbers  $S > 0.9$  in most conditions. The swirling flow helps stabilise the highly decomposed, wet ammonia flames.
- Increasing either the central fuel jet velocity or the wet air velocity in channels increases the swirl number as a result of the chosen constant thermal power and design space.

- The MDI burner is capable of stabilising wet decomposed ammonia featuring as large as 74% steam-to-air ratio. This is associated with a stoichiometric mixture containing 80% vol decomposed ammonia.
- High H<sub>2</sub>% rich flame interacts with the flow field differently from the low H<sub>2</sub>% lean other cases. It may lead to difficulties in building complex reactor networks for predicting emissions from high H<sub>2</sub>% eFuel combustion.

For the combustion regimes and flame markers, it is found that.

- The reaction zone of the flame with  $\eta = 60\%$ ,  $\Omega = 0.69$ ,  $\phi = 1.0$  is highly distributed. Nearly 80% of the fluid parcels are defined in the MILD regime.
- OH can only be a reasonable marker for thin flames, while it fails to work for distributed flames in the MILD combustion regime.
- The strongly distributed flame characteristics have similarities to those of extinguishing flames (those with  $\eta = 40\%$ ). For the former, swirl stabilised fluid parcels wrap around parcels defined in the MILD regime, while it is the opposite for extinguishing flames.
- For extinguishing flames, more than 50% of fluid parcels are defined in the swirl-stabilised regime.
- NNH is the most accurate flame marker across all possible combinations of NH<sub>3</sub>/N<sub>2</sub>/H<sub>2</sub> fuel blends and at the most interesting combustion conditions.

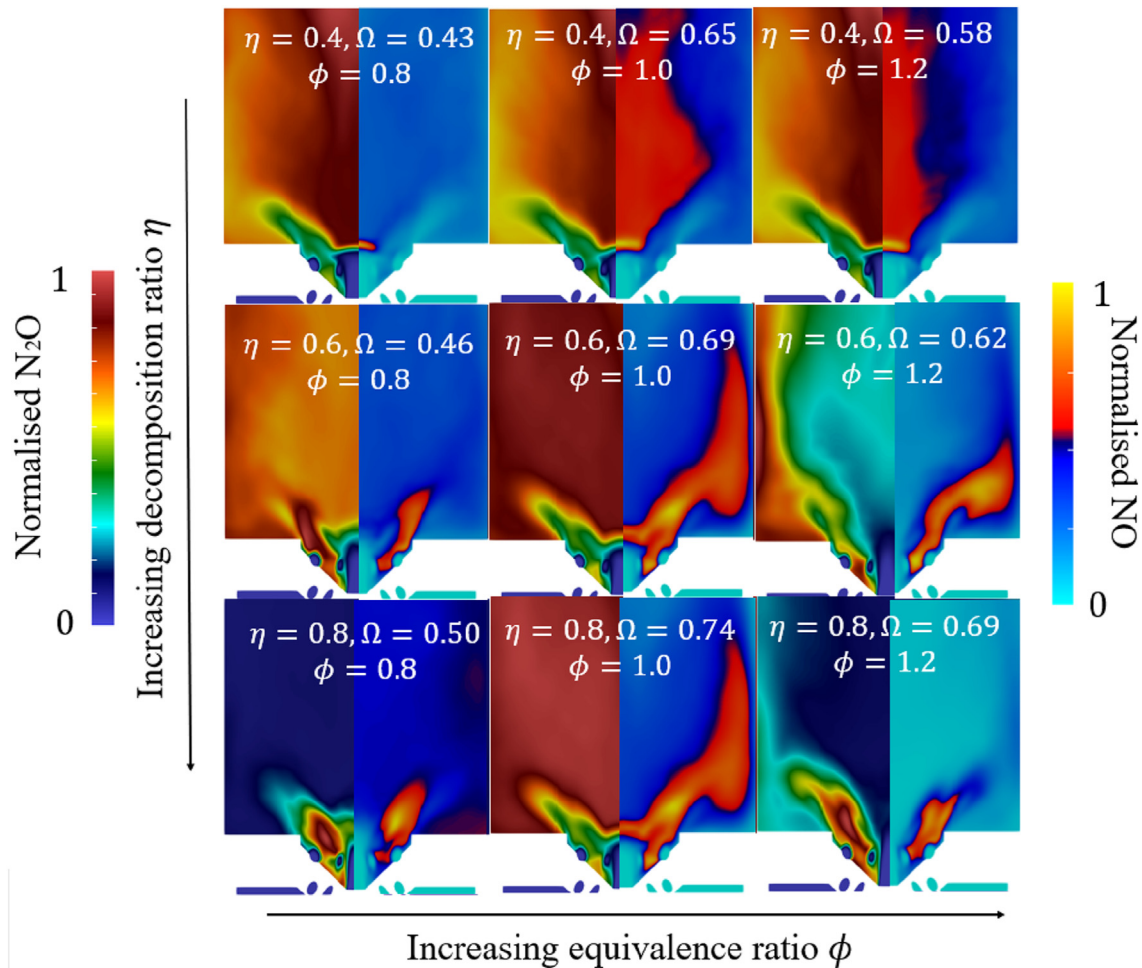


Fig. 11 – Contour plots of normalised  $N_2O$  emission from burning steam-diluted, decomposed ammonia in a 1kW MDI burner. (Clipped to a height where emissions are reported in Fig. 10).

- For flames operating under lean conditions,  $HO_2$ ,  $NH_2$  and  $OH$  are also effective flame makers, while  $OH$  is a bad flame maker for stoichiometric and rich ammonia flame.

For the total emission, it is found.

- Stoichiometric combustion of the highest  $H_2\%$  containing, wettest ammonia flame  $\eta = 0.8, \Omega = 0.74, \phi = 1.0$  emits the lowest pollutants among all cases. The total emission composed of  $NH_3$ ,  $NO$ ,  $NO_2$ , and  $N_2O$  is only slightly above  $400\text{ppmvd}@15\%O_2$ .
- Lean combustion of steam-diluted, decomposed ammonia is not suggested that the total emission is in general unacceptable.

Other than these, an important finding must be highlighted that the combustion regime seems to have a very strong impact on the near-wall  $N_2O$  formation. Suggestions are given that for burning eFuels in the MILD regime, good heat insulation on the chamber wall is the key to the  $N_2O$  emission reduction. However, for burning eFuels in the conventional regimes, the impact of wall heat loss is insignificant.

Overall, the present work for the first time provides insights into the steam-diluted, decomposed ammonia flame characteristics. The research findings suggest that the MDI burner can be a suitable candidate for flexible ammonia power conversion featuring all the four advantages previously introduced.

#### CRediT authorship contribution statement

**Kai Zhang:** Methodology, Formal analysis, Investigation, Writing - original draft, Writing - review & editing. **Yazhou Shen:** Writing - review & editing. **Rahul Palulli:** Writing - review & editing. **Ali Ghobadian:** Writing - review & editing. **Jamshid Nouri:** Writing - review & editing. **Christophe Duwig:** Methodology, Conceptualization, Writing - review & editing, Supervision, Funding acquisition.

#### Declaration of competing interest

The authors declare that they have no known competing financial interests or personal relationships that could have appeared to influence the work reported in this paper.

## Acknowledgements

The simulations were performed on resources provided by the Swedish National Infrastructure for Computing (SNIC) at NSC, HPC2N and PDC super-computing centres.

## Appendix A. Supplementary data

Supplementary data to this article can be found online at <https://doi.org/10.1016/j.ijhydene.2023.01.091>.

## REFERENCES

- Valera-Medina A, Xiao H, Owen-Jones M, David WI, Bowen PJ. Ammonia for power. *Prog Energy Combust Sci* 2018;69:63–102.
- Dai L, Gersen S, Glarborg P, Levinsky H, Mokhov A. Experimental and numerical analysis of the autoignition behavior of NH<sub>3</sub> and NH<sub>3</sub>/H<sub>2</sub> mixtures at high pressure. *Combust Flame* 2020;215:134–44.
- Kanoshima R, Hayakawa A, Kudo T, Okafor EC, Colson S, Ichikawa A, Kudo T, Kobayashi H. Effects of initial mixture temperature and pressure on laminar burning velocity and Markstein length of ammonia/air premixed laminar flames. *Fuel* 2022;310:122149.
- Kobayashi H, Hayakawa A, Somarathne KKA, Okafor EC. Science and technology of ammonia combustion. *Proc Combust Inst* 2019;37(1):109–33.
- Sorrentino G, Sabia P, Bozza P, Ragucci R, de Joannon M. Low-NO<sub>x</sub> conversion of pure ammonia in a cyclonic burner under locally diluted and preheated conditions. *Appl Energy* 2019;254:113676.
- Shen Y, Zhang K, Duwig C. Investigation of wet ammonia combustion characteristics using LES with finite-rate chemistry. *Fuel* 2022;311:122422.
- Nozari H, Karaca G, Tuncer O, Karabeyoglu A. Porous medium based burner for efficient and clean combustion of ammonia–hydrogen–air systems. *Int J Hydrogen Energy* 2017;42(21):14775–85.
- Ni S, Zhao D. NO<sub>x</sub> emission reduction in ammonia-powered micro-combustors by partially inserting porous medium under fuel-rich condition. *Chem Eng J* 2022:134680.
- Božo MG, Mashruk S, Zitouni S, Valera-Medina A. Humidified ammonia/hydrogen RQL combustion in a trigeneration gas turbine cycle. *Energy Convers Manag* 2021;227:113625.
- Mashruk S, Xiao H, Valera-Medina A. Rich-Quench-Lean model comparison for the clean use of humidified ammonia/hydrogen combustion systems. *Int J Hydrogen Energy* 2021;46(5):4472–84.
- Zhang K, Shen Y, Duwig C. Finite rate simulations and analyses of wet/distributed flame structure in swirl-stabilized combustion. *Fuel* 2021;289:119922.
- Rocha RC, Costa M, Bai XS. Combustion and emission characteristics of ammonia under conditions relevant to modern gas turbines. *Combust Sci Technol* 2021;193(14):2514–33.
- Sorrentino G, Sabia P, Ariemma GB, Ragucci R, de Joannon M. Reactive structures of ammonia MILD combustion in diffusion ignition processes. *Front Energy Res* 2021:659.
- Mohammadpour A, Mazaheri K, Alipoor A. Reaction zone characteristics, thermal performance and NO<sub>x</sub>/N<sub>2</sub>O emissions analyses of ammonia MILD combustion. *Int J Hydrogen Energy* 2022;47(48):21013–31.
- Sorrentino G, Cavaliere A, Sabia P, Ragucci R, De Joannon M. Diffusion ignition processes in MILD combustion: a mini-review. *Front Mech Eng* 2020;6:10.
- Zhang X, Moosakutty SP, Rajan RP, Younes M, Sarathy SM. Combustion chemistry of ammonia/hydrogen mixtures: jet-stirred reactor measurements and comprehensive kinetic modeling. *Combust Flame* 2021;234:111653.
- Manna MV, Sabia P, Sorrentino G, Viola T, Ragucci R, de Joannon M. New insight into NH<sub>3</sub>-H<sub>2</sub> mutual inhibiting effects and dynamic regimes at low-intermediate temperatures. *Combust Flame* 2022:111957.
- Okafor EC, Somarathne KKA, Hayakawa A, Kudo T, Kurata O, Iki N, Kobayashi H. Towards the development of an efficient low-NO<sub>x</sub> ammonia combustor for a micro gas turbine. *Proc Combust Inst* 2019;37(4):4597–606.
- Valera-Medina A, Marsh R, Runyon J, Pugh D, Beasley P, Hughes T, Bowen P. Ammonia–methane combustion in tangential swirl burners for gas turbine power generation. *Appl Energy* 2017;185:1362–71.
- Wojtowicz MA, Pels JR, Moulijn JA. Combustion of coal as a source of N<sub>2</sub>O emission. *Fuel Process Technol* 1993;34(1):1–71.
- Mashruk S, Kovaleva M, Tung Chong C, Hayakawa A, Okafor EC, Valera-Medina A. Nitrogen oxides as a by-product of ammonia/hydrogen combustion regimes. *Chemical Engineering Transactions* 2021;89:613–8.
- Mashruk S, Okafor EC, Kovaleva M, Alnasif A, Pugh D, Hayakawa A, Valera-Medina A. Evolution of N<sub>2</sub>O production at lean combustion condition in NH<sub>3</sub>/H<sub>2</sub>/air premixed swirling flames. *Combust Flame* 2022;244:112299.
- Hayakawa A, Hayashi M, Gotama GJ, Kovaleva M, Okafor EC, Colson S, Kudo T, Mashruk S, Valera-Medina A, Kobayashi H. N<sub>2</sub>O production Characteristics of ammonia/hydrogen/air premixed laminar flames Stabilized in stagnation Flows at lean conditions. In: 13<sup>th</sup> asia-pacific conference on combustion 2021; 2021.
- Ariemma GB, Sabia P, Sorrentino G, Bozza P, De Joannon M, Ragucci R. Influence of water addition on MILD ammonia combustion performances and emissions. *Proceedings of the combustion Institute* 2021;vol. 38(4):5147–54.
- Pugh D, Bowen P, Valera-Medina A, Giles A, Runyon J, Marsh R. Influence of steam addition and elevated ambient conditions on NO<sub>x</sub> reduction in a staged premixed swirling NH<sub>3</sub>/H<sub>2</sub> flame. *Proc Combust Inst* 2019;37(4):5401–9.
- Okafor EC, Naito Y, Colson S, Ichikawa A, Kudo T, Hayakawa A, Kobayashi H. Experimental and numerical study of the laminar burning velocity of CH<sub>4</sub>–NH<sub>3</sub>–air premixed flames. *Combust Flame* 2018;187:185–98.
- Okafor EC, Tsukamoto M, Hayakawa A, Somarathne KKA, Kudo T, Tsujimura T, Kobayashi H. Influence of wall heat loss on the emission characteristics of premixed ammonia-air swirling flames interacting with the combustor wall. *Proceedings of the combustion Institute* 2021;vol. 38(4):5139–46.
- Ariemma GB, Sorrentino G, Ragucci R, de Joannon M, Sabia P. Ammonia/Methane combustion: stability and NO<sub>x</sub> emissions. *Combust Flame* 2022;241:112071.
- Ariemma GB, Bozza P, de Joannon M, Sabia P, Sorrentino G, Ragucci R. Alcohols as energy carriers in MILD combustion. *Energy Fuels* 2021;35(9):7253–64.
- Sabia P, Sorrentino G, Ariemma GB, Manna MV, Ragucci R, de Joannon M. MILD combustion and biofuels: a minireview. *Energy Fuels* 2021;35(24):19901–19.
- Shen Y, Ghulam M, Zhang K, Gutmark E, Duwig C. Vortex breakdown of the swirling flow in a Lean Direct Injection burner. *Phys Fluids* 2020;32(12):125118.

- [33] Yellugari K, Ghulam MM, Shen Y, Villalva Gomez R, Gutmark EJ. Effect of nozzle spacing on flow behavior in a lean direct injection combustor. In: AIAA scitech 2021 forum; 2021. 0292.
- [34] Ghulam MM, Shen Y, Baier F, Gomez RV, Gutmark EJ, Duwig C. Characterization of non-reacting swirling flow in a gas turbine fuel injector. In: AIAA scitech 2021 forum; 2021. p. 1109.
- [35] Dolan B, Villalva R, Munday D, Zink G, Pack S, Gutmark E. Flame dynamics in a multi-nozzle staged combustor during high power operation. In: *Turbo expo: Power for land, sea, and air*. vol. 45691. American Society of Mechanical Engineers; 2014, June. V04BT04A019.
- [36] Dolan B, Gomez RV, Zink G, Pack S, Gutmark E. Effect of nozzle spacing on nitrogen-oxide emissions and lean operability. *AIAA J* 2016;54(6):1953–61.
- [37] Dolan B, Gomez RV, Gutmark E. Optical measurements of interacting lean direct injection fuel nozzles with varying spacing. In: *Turbo expo: Power for land, sea, and air*. vol. 56697. American Society of Mechanical Engineers; 2015, June. V04BT04A051.
- [38] Dolan B, Villalva Gomez R, Munday D, Gutmark E, Zink G, Pack S, Goeke J. OH\* chemiluminescence in a multipoint combustion system: steady state and limit cycle behavior. In: 51<sup>st</sup> AIAA aerospace sciences meeting including the new horizons forum and aerospace exposition; 2013. p. 560.
- [39] Cheng M, Wang H, Xiao H, Luo K, Fan J. Emission characteristics and heat release rate surrogates for ammonia premixed laminar flames. *Int J Hydrogen Energy* 2021;46(24):13461–70.
- [40] Zhu X, Guiberti TF, Li R, Roberts WL. Numerical study of heat release rate markers in laminar premixed Ammonia-methane-air flames. *Fuel* 2022;318:123599.
- [41] Zhang H, Han X, Jiang J, Li X, Gan X, Zhou B. Numerical study of experimental feasible heat release rate markers for NH<sub>3</sub>-H<sub>2</sub>-air premixed flames. *Int J Hydrogen Energy* 2022;47(65):28165–75.
- [42] Architects Of Openfoam. [online] CFD direct. Openfoam V6 user guide: CFD direct. 2022. Available at: <https://cfdirect/openfoam/user-guide-v6/>. [Accessed 10 January 2022].
- [43] Ayachit U. The paraview guide: a parallel visualization application. Kitware, Inc; 2015.
- [44] Zhang K. GitHub. [online] Available at: [https://github.com/WWIWWIWW/Python\\_utilities](https://github.com/WWIWWIWW/Python_utilities). [Accessed 8 June 2022].
- [45] Zhang K, Shen Y, Duwig C. Identification of coherent structures in distributed swirl-stabilized wet combustion. *Fuel* 2021;296:120685.
- [46] Duwig C, Iudiciani P. Large Eddy Simulation of turbulent combustion in a stagnation point reverse flow combustor using detailed chemistry. *Fuel* 2014;123:256–73.
- [47] Duwig C, Dunn MJ. Large Eddy Simulation of a premixed jet flame stabilized by a vitiated co-flow: evaluation of auto-ignition tabulated chemistry. *Combust Flame* 2013;160(12):2879–95.
- [48] Chemical Mechanism: Combustion Research Group at UC San Diego. [online] Available at: <https://web.eng.ucsd.edu/mae/groups/combustion/mechanism.html>. [Accessed 23 January 2022].
- [49] Jiang Y, Gruber A, Seshadri K, Williams F. An updated short chemical-kinetic nitrogen mechanism for carbon-free combustion applications. *Int J Energy Res* 2020;44(2):795–810.
- [50] Fooladgar E, Toth P, Duwig C. Characterization of flameless combustion in a model gas turbine combustor using a novel post-processing tool. *Combust Flame* 2019;204:356–67.
- [51] Duwig C, Nogenmyr KJ, Chan CK, Dunn MJ. Large eddy simulations of a piloted lean premix jet flame using finite-rate chemistry. *Combust Theor Model* 2011;15(4):537–68.
- [52] Nicoud F, Ducros F. Subgrid-scale stress modelling based on the square of the velocity gradient tensor. *Flow, Turbul Combust* 1999;62(3):183–200.
- [53] Trisjono P, Pitsch H. Systematic analysis strategies for the development of combustion models from DNS: a review. *Flow, Turbul Combust* 2015;95(2):231–59.
- [54] Zhang K, Dybe S, Shen Y, Schimek S, Paschereit CO, Duwig C. Experimental and numerical investigation of ultra-wet methane combustion technique for power generation. In: *Turbo expo: Power for land, sea, and air*. vol. 84133. American Society of Mechanical Engineers; 2020, September. V04BT04A049.
- [55] Issa RI. Solution of the implicitly discretised fluid flow equations by operator-splitting. *J Comput Phys* 1986;62(1):40–65.
- [56] Solana-Perez R, Shcherbanev SA, Ciani A, Noiray N. Effect of mixing on the anchoring and combustion Regimes of pure hydrogen Flames in sequential combustors. In: *Turbo expo: Power for land, sea, and air*. vol. 85994. American Society of Mechanical Engineers; 2022, June. V03AT04A021.
- [57] Elbaz AM, Wang S, Guiberti TF, Roberts WL. Review on the recent advances on ammonia combustion from the fundamentals to the applications. *Fuel Communications* 2022:100053.
- [58] Lindstedt RP, Lockwood FC, Selim MA. Detailed kinetic modelling of chemistry and temperature effects on ammonia oxidation. *Combust Sci Technol* 1994;99(4–6):253–76.
- [59] Meyers JL, Well AD. Research design and statistical analysis. 2nd 2003.
- [60] Cavaliere A, De Joannon M. Mild combustion. *Prog Energy Combust Sci* 2004;30(4):329–66.
- [61] Minamoto Y. Physical aspects and modelling of turbulent MILD combustion. Doctoral dissertation, University of Cambridge; 2014.
- [62] Galle M, Agar DW, Watzenberger O. Thermal N<sub>2</sub>O decomposition in regenerative heat exchanger reactors. *Chem Eng Sci* 2001;56(4):1587–95.